Hydrodynamic interactions in polar liquid crystals on evolving surfaces

Ingo Nitschke and Sebastian Reuther*
Institute of Scientific Computing, Technische Universität Dresden, Germany

Axel Voigt
Institute of Scientific Computing, Technische Universität Dresden and Dresden Center for Computational Materials Science (DCMS) and Center for Systems Biology Dresden (CSBD) and Cluster of Excellence Physics of Life (PoL), Dresden, Germany

(Received 31 August 2018; published 8 April 2019)

We consider the derivation and numerical solution of the flow of passive and active polar liquid crystals, whose molecular orientation is subjected to a tangential anchoring on an evolving curved surface. The underlying passive model is a simplified surface Ericksen-Leslie model, which is derived as a thin-film limit of the corresponding three-dimensional equations with appropriate boundary conditions. A finite element discretization is considered and the effect of hydrodynamics on the interplay of topology, geometric properties, and defect dynamics is studied for this model on various stationary and evolving surfaces. Additionally, we consider an active model. We propose a surface formulation for an active polar viscous gel and exemplarily demonstrate the effect of the underlying curvature on the location of topological defects on a torus.

DOI: 10.1103/PhysRevFluids.4.044002

I. INTRODUCTION

Liquid crystals (LCs) are partially ordered materials that combine the fluidity of liquids with the orientational order of crystalline solids [1,2]. Topological defects are a key feature of LCs if considered under external constraints. In particular on curved surfaces these defects are important and have been intensively studied on a sphere [3–8] and under more complicated constraints [9–11]. LCs on curved surfaces can be realized on various levels. One possibility is to prepare a double emulsion of two concentric droplets [12] for which the intervening shell is filled with molecular or colloidal LCs which show planar anchoring at the two curved interfaces [13–15]. Also air bubbles covered by microrods have been prepared and studied in real space [16]. Moreover, topological defects for charged colloidal spheres confined on a sphere were experimentally studied [17]. Ellipsoidal colloids bound to curved fluid-fluid interfaces with negative Gaussian curvature [18] and spherical droplets covered with aspherical surfactants [19] were explored. Even living and motile "particles" like cells [20] and suspensions of microtubules and kinesin [21,22] were recently studied on surfaces with nonconstant curvature. In all these studies a tight coupling between topology, geometric properties, and defect dynamics is observed. In equilibrium, defects are positioned according to geometric properties of the surface [23–25]. Creation and annihilation of defects can result from geometric interaction, leading to different realizations of the Poincaré-Hopf theorem on topologically equivalent but geometrically different surfaces [26]. Also changes in the phase diagram can be induced by the geometry, e.g., allowing for coexistence of isotropic and nematic phases in surface LCs [27]. In active systems the observed phenomena are even richer,

*Corresponding author: sebastian.reuther@tu-dresden.de

including, e.g., oscillating defect patterns [21,28] and circulating band structures [29]. The effect of hydrodynamics on these phenomena is more or less unexplored.

Most of the theoretical studies of these phenomena use particle methods. Despite the interest in such methods a continuous description would be more essential for predicting and understanding the macroscopic relation between type and position of the defects and geometric properties of the surface. Also the influence of hydrodynamics and dynamic shape changes on these relations would be much more appropriate to study within a continuous approach. However, a coherent model, which accounts for the complex interplay between topology, geometry, defect interactions, hydrodynamics, and shape changes, is still lacking. In [30], an attempt in this direction is proposed but for a fixed surface. We here extend this approach and propose a minimal continuous surface hydrodynamic LC model, which contains the evolution of the surface, tangential polar ordering, and surface hydrodynamics. The passive model is derived as a thin-film limit of the simplified Ericksen-Leslie model [31]. We describe a numerical approach to solve this model on general surfaces and demonstrate by simulations various expected and some unexpected phenomena on ellipsoidal and toroidal surfaces. These phenomena result from the tight coupling of the geometry with the fluid velocity and the director field. However, a full exploration of the rich nonlinear phenomena resulting from these relations goes beyond the scope of the paper. This also holds for the extension to active systems. The proposed model of surface active polar viscous gels follows as a thin-film limit of a three-dimensional active polar viscous gel model, which combines a more general Ericksen-Leslie model with active components [32,33]. The model can be derived and numerically solved using the same concepts. We here only formulate the model and exemplarily demonstrate numerically the effect of the underlying curvature on the location of topological defects in an active system. Throughout the whole paper we consider the evolution of the surface to be prescribed and the surface to be decoupled from the surrounding bulk phases in order to highlight the surface hydrodynamics and its coupling with topological and geometric effects.

II. THE ERICKSEN-LESLIE MODEL

The Ericksen-Leslie model [34–36] is an established model for LCs, whose relaxation dynamics are affected by hydrodynamics. In [31] a simplified model was introduced and analyzed. This system already retains the main properties of the original Ericksen-Leslie model [37–40] and will be considered as a starting model to derive a surface hydrodynamic LC model by means of a thin-film limit: see Appendix B. The resulting simplified surface Ericksen-Leslie model [cf. Eqs. (B30)–(B32)] reads

$$\begin{aligned}\pi_{\mathcal{S}}\partial_t \mathbf{v} + \boldsymbol{\nabla}^{\mathcal{S}}_{\mathbf{v}}\mathbf{v} - v_n(\mathcal{B}\mathbf{v} + \nabla_{\mathcal{S}} v_n) &= -\nabla_{\mathcal{S}} p_{\mathcal{S}} + \nu(-\boldsymbol{\Delta}^{\mathrm{dR}}\mathbf{v} + 2\kappa\mathbf{v} + \nabla_{\mathcal{S}}(v_n\mathcal{H}) - 2\,\mathrm{div}_{\mathcal{S}}\,(v_n\mathcal{B})) \\ &\quad - \lambda\,\mathrm{div}_{\mathcal{S}}\,\boldsymbol{\sigma}^{\mathrm{E}}_{\mathcal{S}}, \qquad (1)\\ \mathrm{div}_{\mathcal{S}}\,\mathbf{v} &= v_n\mathcal{H}, \qquad (2)\\ \pi_{\mathcal{S}}\partial_t \mathbf{p} + \boldsymbol{\nabla}^{\mathcal{S}}_{\mathbf{v}}\mathbf{p} &= \eta(\boldsymbol{\Delta}^{\mathrm{DG}}\mathbf{p} - \mathcal{B}^2\mathbf{p}) - \omega_n\big(\|\mathbf{p}\|^2_{\mathcal{S}} - 1\big)\mathbf{p}, \qquad (3)\end{aligned}$$

where $\mathbf{v}(t) \in \mathsf{T}\mathcal{S}(t)$ denotes the tangential surface velocity, $\mathbf{p}(t) \in \mathsf{T}\mathcal{S}(t)$ the tangential director field, representing the averaged molecular orientation, $p_{\mathcal{S}}(\mathbf{x}, t) \in \mathbb{R}$ the surface pressure, and $\boldsymbol{\sigma}^{\mathrm{E}}_{\mathcal{S}} = (\nabla_{\mathcal{S}}\mathbf{p})^T\nabla_{\mathcal{S}}\mathbf{p} + (\mathcal{B}\mathbf{p}) \otimes (\mathcal{B}\mathbf{p})$ the extrinsic surface Ericksen stress tensor. The model is defined on a compact smooth Riemannian surface $\mathcal{S}(t)$. We consider initial conditions $\mathbf{v}(\mathbf{x}, t = 0) = \mathbf{v}_0(\mathbf{x}) \in \mathsf{T}_{\mathbf{x}}\mathcal{S}(0)$ and $\mathbf{p}(\mathbf{x}, t = 0) = \mathbf{p}_0(\mathbf{x}) \in \mathsf{T}_{\mathbf{x}}\mathcal{S}(0)$. The positive constants ν, λ, and η denote the fluid viscosity, the competition between kinetic and elastic potential energy, and the elastic relaxation time for the molecular orientation field, respectively. κ is the Gaussian curvature, $\mathcal{H}$ the mean curvature, $\mathcal{B}$ the shape operator, v_n a prescribed normal velocity of the surface, and ω_n a penalization parameter to enforce $\|\mathbf{p}\| = 1$ weakly. $\mathsf{T}_{\mathbf{x}}\mathcal{S}(t)$ is the tangent space on $\mathbf{x} \in \mathcal{S}(t)$, $\mathsf{T}\mathcal{S}(t) = \sqcup_{\mathbf{x}\in\mathcal{S}(t)}\mathsf{T}_{\mathbf{x}}\mathcal{S}(t)$ the tangent bundle, $\pi_{\mathcal{S}}$ the projection to the tangential space with respect to (w.r.t.) the surface $\mathcal{S}(t)$, and $\boldsymbol{\nabla}^{\mathcal{S}}_{\mathbf{v}}$, $\nabla_{\mathcal{S}}$, $\mathrm{div}_{\mathcal{S}}$, $\boldsymbol{\Delta}^{\mathrm{dR}}$, and $\boldsymbol{\Delta}^{\mathrm{DG}}$ are the covariant directional derivative, covariant gradient, surface

divergence, Laplace–de Rham operator, and Bochner Laplacian, respectively. The system combines an incompressible surface Navier-Stokes equation [41–44] with a weak surface Frank-Oseen model [26] on an evolving surface. For a general discussion on transport of vector-valued quantities on evolving surfaces we refer the reader to [45]. The used formulation with the projection operator $\pi_{\mathcal{S}}$ requires the presence of an embedding space, which is $\mathbb{R}^3$ in our case; see Appendix B for details.

For $\lambda = 0$ Eqs. (1) and (2) are the surface Navier-Stokes equation for an incompressible surface fluid on an evolving surface. These equations can be obtained as a thin-film limit of the three-dimensional Navier-Stokes equation in an evolving domain [44] or by a variational derivation [42]. If only a stationary surface is considered, i.e., $v_n = 0$, the equations reduce to the incompressible surface Navier-Stokes equation as considered in [41,46–51]. Compared with its counterpart in flat space, not only are the operators replaced by the corresponding surface operators, also an additional contribution from the Gaussian curvature arises. This additional term results from the surface divergence of the surface strain rate tensor; see [43,48]. The unusual sign results from the definition of the surface Laplace–de Rham operator [52]. Equation (3) with $\mathbf{v} = \mathbf{0}$, $v_n = 0$ and the Laplace–de Rham operator $\boldsymbol{\Delta}^{\mathrm{dR}}$ instead of the Bochner Laplacian $\boldsymbol{\Delta}^{\mathrm{DG}}$ has been derived as a thin-film limit in [26] and models the L^2-gradient flow of a weak surface Frank-Oseen energy. The different operators result from different one-constant approximations in the Frank-Oseen energy; see Appendix B for details. Again an additional geometric term enters in this equation if compared with the corresponding model in flat space. The term with the shape operator $\mathcal{B}$ results from the influence of the embedding [8,26,53]. The coupled system (1)–(3) with $v_n = 0$ can be considered as the surface counterpart of the model in [31]. Related surface models have been proposed and analyzed in [30,54]. The model in [54] is derived from a variational principle on a stationary surface and thus only contains intrinsic terms. It differs from Eqs. (1)–(3) with $v_n = 0$ by the extrinsic term $\mathcal{B}^2\mathbf{p}$ and the extrinsic contribution in the surface Ericksen stress tensor $(\mathcal{B}\mathbf{p}) \otimes (\mathcal{B}\mathbf{p})$. The model in [30] coincides with our formulation with $v_n = 0$ if a specific parameter set is considered; see also [55]. However, note that in their notation the symbol $\tilde{\nabla}_{\mathcal{S}}$ denotes the surface gradient operator, while we use $\nabla_{\mathcal{S}}$ as the covariant gradient operator. Both are related to each other by $\nabla_{\mathcal{S}}\mathbf{p} + \boldsymbol{\nu} \otimes \mathcal{B}\mathbf{p} = \tilde{\nabla}_{\mathcal{S}}\mathbf{p}$, where $\boldsymbol{\nu}$ denotes the surface normal.

III. NUMERICAL METHOD

Equations (1)–(3) are a system of vector-valued surface partial differential equations (PDEs). Numerical approaches were developed for such equations on general surfaces only recently; see [51,56] for the surface (Navier-)Stokes equation, [26] for the surface Frank-Oseen model, [57] for a surface vector-Laplace equation, and [58] for general surface PDEs. Earlier approaches using vector spherical harmonics, e.g., [26,59,60], are restricted to a sphere or radial manifold shapes [61], and approaches which rewrite the surface Navier-Stokes equation in a surface vorticity-stream function formulation [41,49,62,63] are limited to surfaces with genus $g(S) = 0$; see [50,51] for details. For the numerical solution of Eqs. (1)–(3) we combine the methods in [26,51] in an operator splitting approach. The idea behind these methods is to extend the variational space from vectors in $\mathsf{T}\mathcal{S}$ to vectors in $\mathbb{R}^3$, while penalizing the normal components. This allows one to split the vector-valued surface PDE into a set of coupled scalar-valued surface PDEs for each component for which established numerical methods are available; see the review [64].

The corresponding extended problem to Eqs. (1)–(3) reads

$$\begin{aligned}\pi_{\mathcal{S}}\partial_t\widehat{\mathbf{v}} + \nabla^{\mathcal{S}}_{\widehat{\mathbf{v}}}\widehat{\mathbf{v}} - v_n(\mathcal{B}\widehat{\mathbf{v}} + \nabla_{\mathcal{S}}v_n) &= -\nabla_{\mathcal{S}}p_{\mathcal{S}} + \nu(-\widehat{\boldsymbol{\Delta}}^{\mathrm{dR}}\widehat{\mathbf{v}} + 2\kappa\widehat{\mathbf{v}} + \nabla_{\mathcal{S}}(v_n\mathcal{H}) - 2\,\mathrm{div}_{\mathcal{S}}(v_n\mathcal{B})) \\ &\quad - \lambda\,\mathrm{div}_{\mathcal{S}}\,\widehat{\boldsymbol{\sigma}}^{\mathrm{E}}_{\mathcal{S}} - \alpha_{\mathbf{v}}(\widehat{\mathbf{v}}\cdot\boldsymbol{\nu})\boldsymbol{\nu}, \qquad (4)\\ \mathrm{div}_{\mathcal{S}}\,\widehat{\mathbf{v}} &= v_n\mathcal{H}, \qquad (5)\\ \pi_{\mathcal{S}}\partial_t\widehat{\mathbf{p}} + \nabla^{\mathcal{S}}_{\widehat{\mathbf{v}}}\widehat{\mathbf{p}} &= \eta\big(\widehat{\boldsymbol{\Delta}}^{\mathrm{DG}}\widehat{\mathbf{p}} - \mathcal{B}^2\widehat{\mathbf{p}}\big) - \omega_n(\|\widehat{\mathbf{p}}\|^2 - 1)\widehat{\mathbf{p}} - \alpha_{\mathbf{p}}(\boldsymbol{\nu}\cdot\widehat{\mathbf{p}})\boldsymbol{\nu}, \qquad (6)\end{aligned}$$

with $\widehat{\mathbf{v}} = \widehat{v}_x\,\mathbf{e}^x + \widehat{v}_y\,\mathbf{e}^y + \widehat{v}_z\,\mathbf{e}^z$, $\widehat{\mathbf{p}} = \widehat{p}_x\,\mathbf{e}^x + \widehat{p}_y\,\mathbf{e}^y + \widehat{p}_z\,\mathbf{e}^z \in \mathbb{R}^3$, and $\widehat{\boldsymbol{\sigma}}^{\mathrm{E}}_{\mathcal{S}} = (\nabla_{\mathcal{S}}\widehat{\mathbf{p}})^T\nabla_{\mathcal{S}}\widehat{\mathbf{p}} + (\mathcal{B}\widehat{\mathbf{p}}) \otimes (\mathcal{B}\widehat{\mathbf{p}})$. We further use $\mathrm{div}_{\mathcal{S}}\,\widehat{\mathbf{v}} = \nabla\cdot\widehat{\mathbf{v}} - \boldsymbol{\nu}\cdot(\nabla\widehat{\mathbf{v}}\cdot\boldsymbol{\nu})$, $\mathrm{rot}_{\mathcal{S}}\,\widehat{\mathbf{v}} = -\,\mathrm{div}_{\mathcal{S}}(\boldsymbol{\nu}\times\widehat{\mathbf{v}})$, and $\widehat{\boldsymbol{\Delta}}^{\mathrm{DG}}\widehat{\mathbf{p}} = \mathrm{div}_{\mathcal{S}}\,\nabla_{\mathcal{S}}\widehat{\mathbf{p}}$

and $\widehat{\boldsymbol{\Delta}}^{\mathrm{dR}}\widehat{\mathbf{v}} = -[\mathrm{rot}_{\mathcal{S}}\,\mathrm{rot}_{\mathcal{S}}\,\widehat{\mathbf{v}} + \nabla_{\mathcal{S}}(v_n\mathcal{H})]$ since $\mathrm{div}_{\mathcal{S}}\,\widehat{\mathbf{v}} = v_n\mathcal{H}$. The normal components $\widehat{\mathbf{v}}\cdot\boldsymbol{\nu}$ and $\widehat{\mathbf{p}}\cdot\boldsymbol{\nu}$ are penalized by the additional terms $\alpha_{\mathbf{v}}(\boldsymbol{\nu}\cdot\widehat{\mathbf{v}})\boldsymbol{\nu}$ and $\alpha_{\mathbf{p}}(\boldsymbol{\nu}\cdot\widehat{\mathbf{p}})\boldsymbol{\nu}$ with penalization parameters $\alpha_{\mathbf{v}}$ and $\alpha_{\mathbf{p}}$. For convergence results in $\alpha_{\mathbf{v}}$ and $\alpha_{\mathbf{p}}$ for the surface Navier-Stokes and the surface Frank-Oseen problem we refer the reader to [26,51]. Without these penalization terms the system of equations (4)–(6) is an underdetermined problem, since the vector fields are considered in $\mathbb{R}^3$ and therefore the normal components are completely arbitrary; see [26,51] for details. Equations (4)–(6) can now be solved for each component $\widehat{v}_x$, $\widehat{v}_y$, $\widehat{v}_z$, $\widehat{p}_x$, $\widehat{p}_y$, $\widehat{p}_z$, and $p_{\mathcal{S}}$ using standard approaches for scalar-valued problems on surfaces, such as the surface finite element method [64–66], level set approaches [67–70], or diffuse interface approximations [71]. We consider a simple operator splitting approach and solve Eqs. (4)–(6) iteratively in each time step, employing the same surface finite element discretizations as in [26,51]. A semi-implicit Euler discretization in time is used. Thereby, the nonlinear transport term in Eq. (4) and the norm-1 penalization term in Eq. (6) are linearized in time by a Taylor-1 expansion, and the transport term in Eq. (6) as well as the term including the surface Ericksen stress tensor in Eq. (4) are coupling terms in the operator splitting scheme. Additionally, we employ an adaptive time-stepping scheme which is based on the combination of changes in the surface Frank-Oseen energy and the Courant-Friedrichs-Lewy (CFL) condition. For more details we refer the reader to Appendix A. The resulting discrete equations are implemented in the finite element method toolbox AMDiS [72,73], where we additionally use a domain decomposition ansatz to efficiently distribute the workload on many cores systems.

IV. RESULTS

In the following simulations we use $\lambda = 0.5$, $\alpha_{\mathbf{v}} = 10^2$, $\omega_n = 10^2$, and $\alpha_{\mathbf{p}} = 10^5$, where all parameters are treated as nondimensional. We compare the solution of Eqs. (4)–(6) (the so-called *wet* case) and the solution of Eq. (6) with $\widehat{\mathbf{v}} = 0$ (the so-called *dry* case). To highlight the differences we take the surface Frank-Oseen energy $\mathcal{F}^{\mathbf{P}}$ and the surface kinetic energy $\mathcal{F}^{\mathrm{kin}}$ into account, which read in the extended form, incorporating the penalization term,

$$\mathcal{F}^{\mathbf{P}} := \int_{\mathcal{S}} \frac{\eta}{2}(\|\nabla_{\mathcal{S}}\widehat{\mathbf{p}}\|^2 + (\mathcal{B}\widehat{\mathbf{p}})^2) + \frac{\omega_n}{4}(\|\widehat{\mathbf{p}}\|^2 - 1)^2 + \frac{\alpha_{\mathbf{p}}}{2}(\widehat{\mathbf{p}}\cdot\boldsymbol{\nu})^2 d\mathcal{S}$$

$$\mathcal{F}^{\mathrm{kin}} := \frac{1}{2}\int_{\mathcal{S}} \widehat{\mathbf{v}}^2 d\mathcal{S}.$$

First, we consider Eqs. (4)–(6) on a stationary, i.e., $v_n = 0$, ellipsoidal shape with major axes parameters $(0.7, 0.7, 1.2)$. We use the trivial solution as initial condition for the velocity and for the director field $\widehat{\mathbf{p}}^0 = \nabla_{\mathcal{S}}\psi^0/\|\nabla_{\mathcal{S}}\psi^0\|$ with $\psi^0 = x_0/10 + x_1 + x_2/10$ and $\mathbf{x} = (x_0, x_1, x_2)^T$ the Euclidean coordinate vector. The latter generates a vector field with two $+1$ defects—to be more precise, a source and a sink defect—and an out-of-equilibrium solution. Furthermore, we use $\nu = 2$, $\eta = 0.6$, and $h_{\mathrm{m}} = 1.32 \times 10^{-2}$, where h_{m} denotes the maximum mesh size. Figure 1 shows the influence of the hydrodynamics on the dynamical evolution of the director field. The two defects, which fulfill the Poincaré-Hopf theorem, evolve towards the geometrically favorable positions of high Gaussian curvature, the director field aligns with the minimal curvature lines of the geometry, and as in flat space the hydrodynamics enhances the evolution towards the equilibrium configuration, which coincides for the dry and the wet case.

In the next example we consider a stationary torus with major radius $R = 2$, minor radius $r = 0.5$, and the x_2 axis as symmetry axis. Again we use the trivial solution as initial condition for the velocity $\widehat{\mathbf{v}}$ and a random (normalized) vector field for the director field $\widehat{\mathbf{p}}$. Here, we use the simulation parameters $\nu = 1$ and $\eta = 0.4$. The maximum mesh size is fixed at $h_{\mathrm{m}} = 2.74 \times 10^{-2}$. All other parameters are equal to those used in Fig. 1. In Fig. 2 we focus on the annihilation of defects in one realization. Figure 2 (top) shows the evolution of the director field $\widehat{\mathbf{p}}$ for the dry and the wet case. Again in the wet case the dynamics is enhanced, which is quantified by the stronger overall

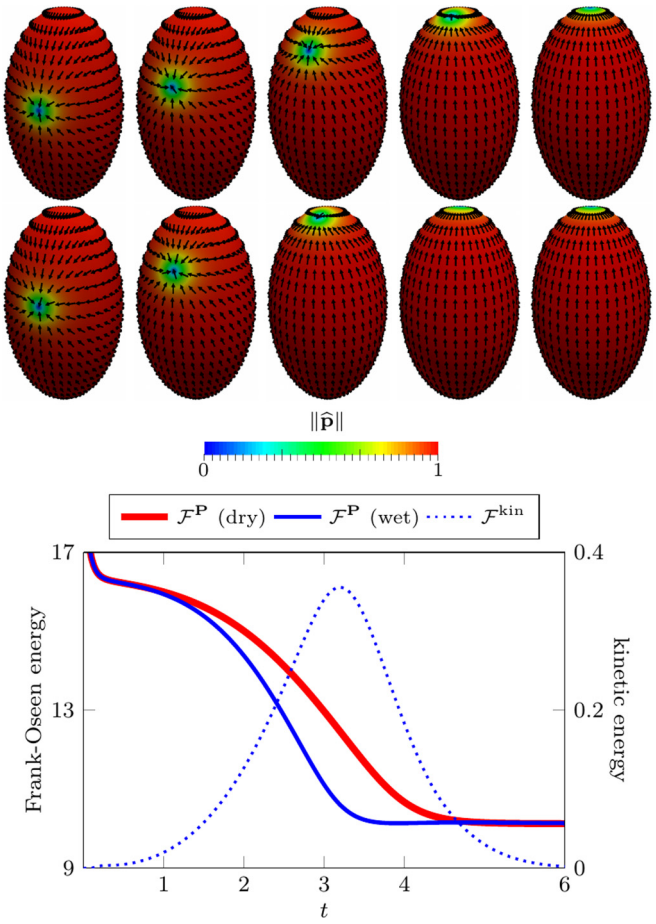

FIG. 1. Top: Evolution of the director field $\widehat{\mathbf{p}}$ on a stationary ellipsoid of the dry case (top row) and the wet case (bottom row) for $t = 1,\ 2,\ 3,\ 4,\ 6$ (left to right). Bottom: Surface Frank-Oseen energy $\mathcal{F}^{\mathbf{P}}$ and surface kinetic energy $\mathcal{F}^{\text{kin}}$ vs time t.

decay of the surface Frank-Oseen energy, cf. Fig. 2 (middle). Additionally, in Fig. 2 (bottom) the corresponding flow field $\widehat{\mathbf{v}}$ is shown for the considered annihilation of a source $(+1)$ and a saddle (-1) defect in the director field $\widehat{\mathbf{p}}$. After all defects are annihilated, which again is in accordance with the Poincaré-Hopf theorem, the velocity field $\widehat{\mathbf{v}}$ decays to zero and the director field $\widehat{\mathbf{p}}$ aligns with the minimal curvature lines of the geometry. The reached equilibrium configuration coincides for both the dry and the wet case.

While in the two previous examples the expected minimal energy configuration was reached, we now consider an initial condition for which only a local minimum can be reached. We use $\widehat{\mathbf{p}}^0 = \nabla_{\mathcal{S}}\psi^0/\|\nabla_{\mathcal{S}}\psi^0\|$ with $\psi^0 = \exp\left[-(\mathbf{x}-\mathbf{m})^2/2\right]$ and $\mathbf{m} = (R, 0, r)^T$ as initial condition for the director field. This produces two ± 1 defect pairs which are located in opposite positions to each other w.r.t. to the symmetry axis of the torus, again fulfilling the Poincaré-Hopf theorem. Thereby, one pair is rotated by an angle of $\pi/2$ compared to the other along the circle with the small radius; see Fig. 3. The parameters are adapted to $\nu = 1$, $\eta = 0.4$, and $h_{\text{m}} = 2.74 \times 10^{-2}$. In a flat geometry with zero curvature these two pairs would annihilate. However, due to the geometric interaction in the present case resulting from the difference of the Gaussian curvature inside and outside of the torus, the reached nontrivial defect configuration is stable and the two ± 1 defect pairs remain over

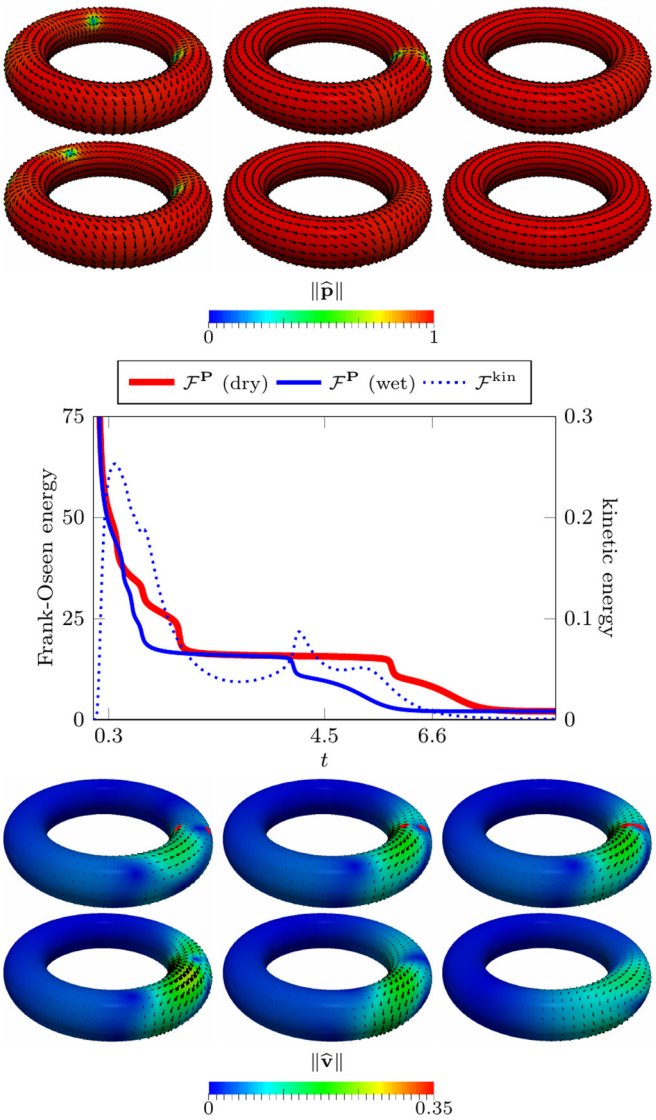

FIG. 2. Top: Evolution of the director field $\widehat{\mathbf{p}}$ on a torus of the dry case (top row) and the wet case (bottom row) for $t = 0.3,\ 4.5,\ 6.6$ (left to right). Middle: Surface Frank-Oseen energy $\mathcal{F}^{\mathbf{P}}$ and surface kinetic energy $\mathcal{F}^{\text{kin}}$ vs time t. Bottom: Velocity field $\widehat{\mathbf{v}}$ for the annihilation of a source $(+1$, left) and a saddle $(-1$, right) defect in the director field $\widehat{\mathbf{p}}$ (red dots) for $t = 3,\ 3.75,\ 3.81,\ 4.05,\ 4.5,\ 5.7$ (left to right and top to bottom).

time. The -1 defects are attracted to regions with negative Gaussian curvature, i.e., the inner of the torus, and $+1$ defects are attracted to regions with positive Gaussian curvature, i.e., the outer of the torus; see Fig. 3. The reached configuration is a local minimum with a significantly larger surface Frank-Oseen energy $\mathcal{F}^{\mathbf{P}}$ as the defect-free configuration. In this example we did not find any significant difference between the dry and the wet case, when the zero initial condition for the velocity $\widehat{\mathbf{v}}$ is used. However, if we use a Killing vector field for the velocity as initial condition, i.e., $\widehat{\mathbf{v}}^0 = 1/2(-x_1, x_0, 0)^T$, cf. [50,51], the four defects start to rotate and cause a damping of the flow field, which converges to zero. In other words, the defects in the director field produce an additional contribution to the total surface stress tensor and therefore the kinetic energy dissipates to zero;

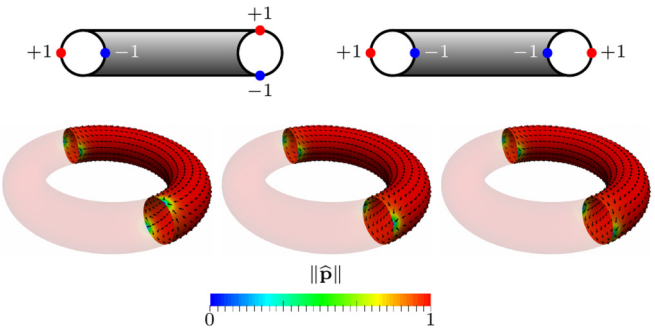

FIG. 3. Top: Schematic defect positions of the initial condition (left) and the final configuration (right) on a torus with the analytical initial condition for the director field $\widehat{\mathbf{p}}$ and zero initial condition for the velocity field $\widehat{\mathbf{v}}$. Red dots indicate $+1$ defects (sources or sinks) and blue dots indicate -1 defects (saddle). Bottom: Evolution of the director field $\widehat{\mathbf{p}}$ for $t = 1,\ 5,\ 25$ (left to right).

see Fig. 4. The final configuration is a rotation of the configuration reached with $\widehat{\mathbf{v}}^0 = 0$, with the rotation angle depending on the strength of the initial velocity and the viscosity.

We now let the ellipsoid from Fig. 1 evolve by prescribing the normal velocity v_n, such that the ellipsoid changes to a sphere and afterwards to an ellipsoid with a different axis orientation and vice versa to obtain a shape oscillation. The surface area remains constant during the evolution. Figure 5 shows schematically the evolution of the geometry and the axes parameters for one period of oscillation. We use the same simulation parameters and initial conditions as considered in Fig. 1. The evolution of the director field $\widehat{\mathbf{p}}$ is shown in Fig. 6, again for the dry (top) and the wet (bottom) case. The defect positions again reallocate at their geometrically favorable position. However, due to the change in the geometry, the timescale for the reallocation competes with the timescale for the shape changes. The enhanced evolution towards the minimal energy configuration with hydrodynamics becomes even more significant in these situations. Already slight modifications of the geometry are enough to push the defect after crossing the sphere configurations (with no preferred defect position) to the energetically favorable state. In the dry case there is a strong delay and much stronger shape changes are needed to push the defect to the energetically favorable position. First an energy barrier

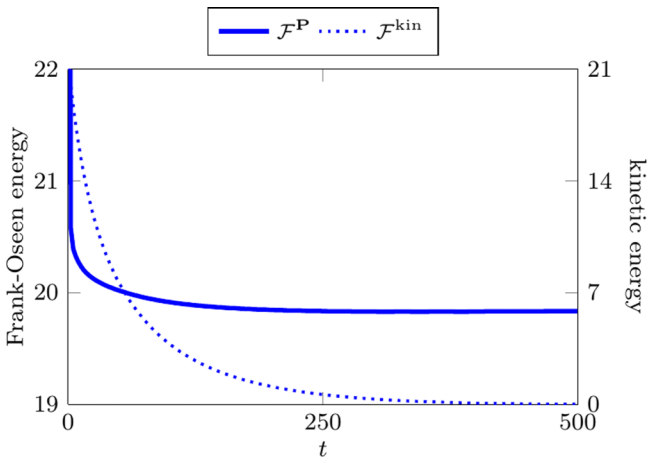

FIG. 4. Surface Frank-Oseen energy $\mathcal{F}^{\mathbf{P}}$ and surface kinetic energy $\mathcal{F}^{\mathrm{kin}}$ vs time t for the analytical initial condition for the director field $\widehat{\mathbf{p}}$ and the killing vector field as initial condition for the velocity $\widehat{\mathbf{v}}$.

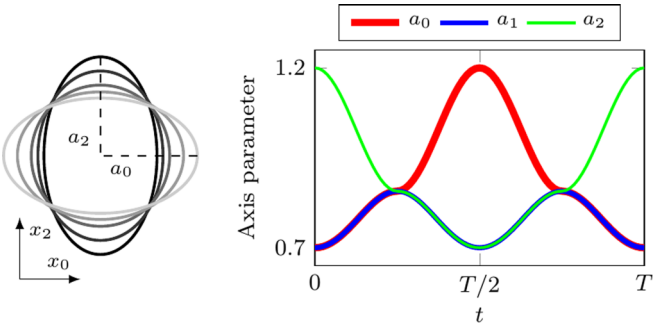

FIG. 5. Left: Schematic description of the ellipsoid evolution for a half period of oscillation. Descending gray scale indicates increasing time. The motion in the second half of the oscillation is reversed, respectively. Right: Major axes parameters for the ellipsoid over a full period of oscillation. The time of one oscillation period is considered to be $T = 160$. The major axes parameters are chosen such that the surface area of the ellipsoid is conserved over time.

for reallocating the defect position has to be overcome, which is shown by the further increase of the red line after the blue line has already dropped after crossing the sphere configuration in Fig. 6 (middle). The parameters and the initial condition are further chosen in such a way that the defects in the dry case not quite reach the position at the poles if the shape evolution crosses the sphere. In the wet case they have moved beyond. This results in a constant orientation in the dry case and a flipping of the orientation of the director field in the wet case in each oscillation. The final configuration in Fig. 6 after completing one oscillation cycle is energetically equivalent for the dry and the wet case even if the orientation of the director field $\widehat{\mathbf{p}}$ differs; see also the video in the Supplemental Material [74]. This behavior clearly depends on the used parameters. However, it also demonstrates the strong influence hydrodynamics might have in such highly nonlinear systems, where the topology, geometric properties, and defect dynamics are strongly coupled.

These examples together with the demonstrated energy reduction by creation of additional defects in geometrically favored positions in [26], which is expected to hold also for the wet case, lead to a very rich phase space, considering geometric and material properties, whose exploration is beyond the scope of this paper.

V. DISCUSSION

Equations (1)–(3) have been derived as a thin-film limit of a three-dimensional simplified Ericksen-Leslie model; see Appendix B. In [54] a similar model was proposed, which differs from Eqs. (1)–(3) with $v_n = 0$ in the extrinsic contributions. Especially the surface Ericksen stress tensor is considered to be $\boldsymbol{\sigma}_{\mathcal{S}}^{\mathrm{E}} = (\nabla_{\mathcal{S}}\mathbf{p})^T \nabla_{\mathcal{S}}\mathbf{p}$. To show the strong difference between this intrinsic and the extrinsic surface Ericksen stress tensor $\boldsymbol{\sigma}_{\mathcal{S}}^{\mathrm{E}} = (\nabla_{\mathcal{S}}\mathbf{p})^T \nabla_{\mathcal{S}}\mathbf{p} + (\mathcal{B}\mathbf{p}) \otimes (\mathcal{B}\mathbf{p})$ considered here and in [30], we come back to the stationary ellipsoid in Fig. 1. We use slightly different parameters, i.e., $\nu = 0.5$, $\eta = 0.3$, and $\lambda = 1$, which lead to a damped oscillation of the defects around the energetically favorable positions before they reach the final state configuration as in Fig. 1. In Fig. 7 the differences in the time evolution of the surface Frank-Oseen energy as well as the surface kinetic energy are shown for the cases of both the intrinsic and extrinsic surface Ericksen stress tensor. The influence of the hydrodynamics is much stronger for the extrinsic surface Ericksen stress. Together with the example in Fig. 6, such differences in the dynamics might have a huge impact on the overall evolution if also shape changes are considered.

All results so far are for the simplified surface Ericksen-Leslie model. However, Appendix B provides all necessary tools to do the thin-film analysis also for more complicated systems, such as more general Ericksen-Leslie models or active versions of them. Here, we provide the formulation for a surface active polar viscous gel; see [32,33] and [75,76] for the considered three-dimensional

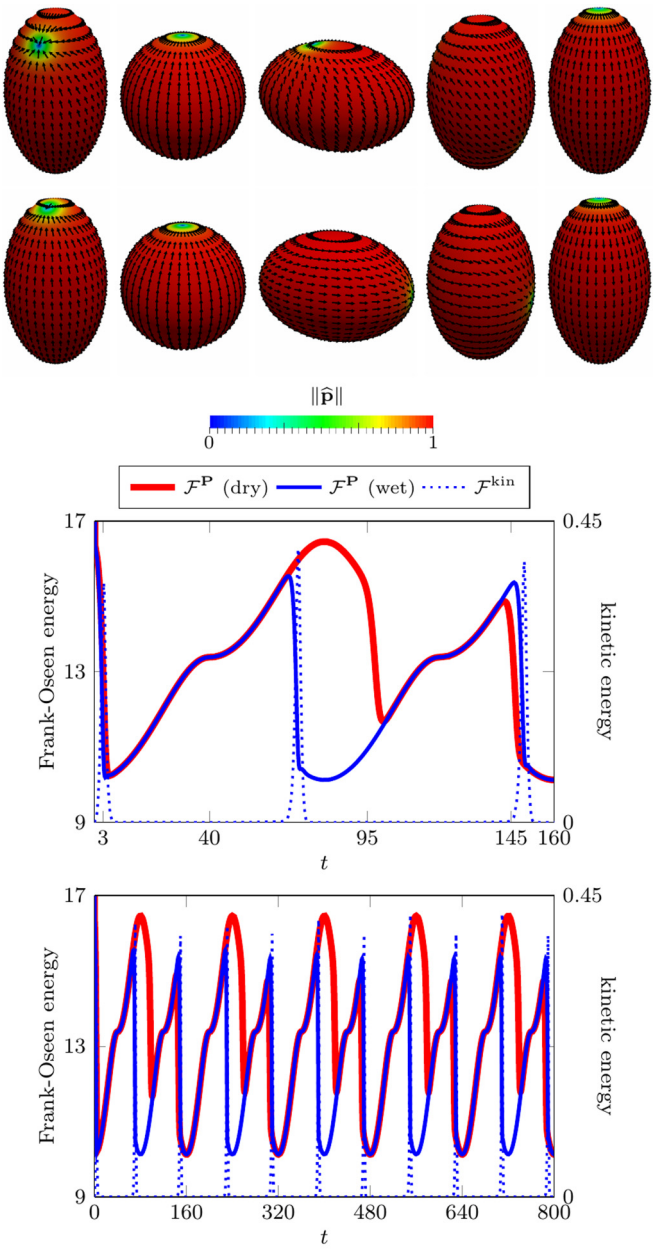

FIG. 6. Top: Evolution of the director field $\widehat{\mathbf{p}}$ on an evolving ellipsoid of the dry case (top row) and the wet case (bottom row) for $t = 3,\ 40,\ 95,\ 145,\ 160$ (left to right). Middle: Surface Frank-Oseen energy $\mathcal{F}^{\mathbf{P}}$ and surface kinetic energy $\mathcal{F}^{\text{kin}}$ vs time t for the first period of oscillation. Bottom: Surface Frank-Oseen energy $\mathcal{F}^{\mathbf{P}}$ and surface kinetic energy $\mathcal{F}^{\text{kin}}$ vs time t over five periods of oscillation.

formulation, which correspond to Eqs. (B1)–(B3) with boundary conditions (B4)–(B6), i.e.,

$$\begin{aligned}
\partial_t \boldsymbol{V} + \nabla_{\boldsymbol{U}} \boldsymbol{V} &= -\nabla P_{\Omega_h} + \nu \boldsymbol{\Delta} \boldsymbol{V} + \operatorname{div} \boldsymbol{\sigma}^{\mathrm{A}} - \lambda \operatorname{div} \boldsymbol{\sigma}^{\mathrm{E}} \\
\operatorname{div} \boldsymbol{V} &= 0, \\
\partial_t \boldsymbol{P} + \nabla_{\boldsymbol{U}} \boldsymbol{P} &= \boldsymbol{H} + \alpha \boldsymbol{D} \boldsymbol{P} + \boldsymbol{\Omega} \boldsymbol{P}
\end{aligned}$$

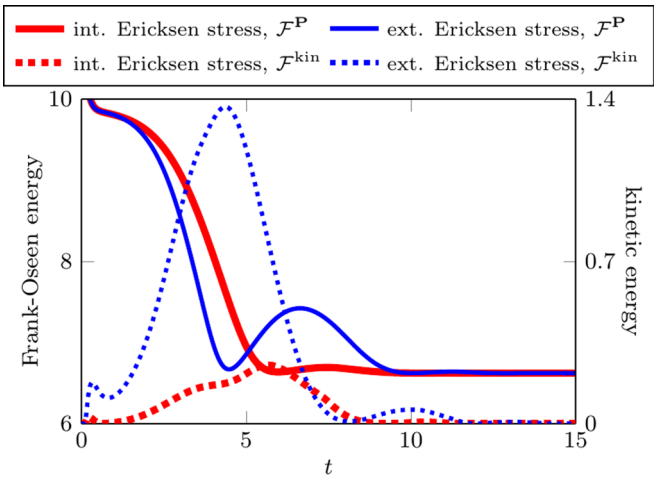

FIG. 7. Surface Frank-Oseen energy $\mathcal{F}^{\mathbf{P}}$ and surface kinetic energy $\mathcal{F}^{\text{kin}}$ vs time t for the simulation with the damped oscillation of the defects around the minimal defect configuration.

with

$$\boldsymbol{\sigma}^{\text{A}} = \frac{1}{2}(\boldsymbol{P}\otimes\boldsymbol{H} - \boldsymbol{H}\otimes\boldsymbol{P}) - \frac{\alpha}{2}(\boldsymbol{P}\otimes\boldsymbol{H} + \boldsymbol{H}\otimes\boldsymbol{P}) + \beta\boldsymbol{P}\otimes\boldsymbol{P},$$
$$\boldsymbol{H} = \eta\boldsymbol{\Delta}\boldsymbol{P} - \omega_n\big(\|\boldsymbol{P}\|^2_{\Omega_h} - 1\big)\boldsymbol{P}, \quad \boldsymbol{D} = \frac{1}{2}(\nabla\boldsymbol{V} + (\nabla\boldsymbol{V})^T), \quad \boldsymbol{\Omega} = \frac{1}{2}(\nabla\boldsymbol{V} - (\nabla\boldsymbol{V})^T),$$

and $\alpha, \beta \in \mathbb{R}$. The Navier-Stokes equation now contains additional distortion and active stresses, combined in $\boldsymbol{\sigma}^{\text{A}}$, while in the director field equation additional contributions from the strain rate tensor $\boldsymbol{D}$ and the vorticity tensor $\boldsymbol{\Omega}$ arise. The corresponding thin-film limit reads

$$\pi_{\mathcal{S}}\partial_t\mathbf{v} + \nabla^{\mathcal{S}}_{\mathbf{v}}\mathbf{v} = v_n(\mathcal{B}\mathbf{v} + \nabla_{\mathcal{S}}v_n) - \nabla_{\mathcal{S}}p_{\mathcal{S}} + \nu(-\boldsymbol{\Delta}^{\text{dR}}\mathbf{v} + 2\kappa\mathbf{v} + \nabla_{\mathcal{S}}(v_n\mathcal{H}) - 2\,\text{div}_{\mathcal{S}}(v_n\mathcal{B}))$$
$$+ \text{div}_{\mathcal{S}}\,\boldsymbol{\sigma}^{\text{A}}_{\mathcal{S}} - \lambda\,\text{div}_{\mathcal{S}}\,\boldsymbol{\sigma}^{\text{E}}_{\mathcal{S}} - \frac{1-\alpha}{2}[\mathbf{p}^T\mathcal{B}(\mathcal{H}\mathbf{v} + \nabla_{\mathcal{S}}v_n)]\mathbf{p} + \frac{1+\alpha}{2}(\mathbf{p}^T\mathcal{B}\mathbf{v})\mathcal{B}\mathbf{p}, \tag{7}$$
$$\text{div}_{\mathcal{S}}\,\mathbf{v} = v_n\mathcal{H}, \tag{8}$$
$$\pi_{\mathcal{S}}\partial_t\mathbf{p} + \nabla^{\mathcal{S}}_{\mathbf{v}}\mathbf{p} = \mathbf{h} + \alpha\boldsymbol{D}_{\mathcal{S}}\mathbf{p} + \boldsymbol{\Omega}_{\mathcal{S}}\mathbf{p} - \alpha v_n\mathcal{B}\mathbf{p} \tag{9}$$

with

$$\boldsymbol{\sigma}^{\text{A}}_{\mathcal{S}} = \tfrac{1}{2}(\mathbf{p}\otimes\mathbf{h} - \mathbf{h}\otimes\mathbf{p}) - \frac{\alpha}{2}(\mathbf{p}\otimes\mathbf{h} + \mathbf{h}\otimes\mathbf{p}) + \beta\mathbf{p}\otimes\mathbf{p},$$
$$\mathbf{h} = \eta(\boldsymbol{\Delta}^{\text{DG}}\mathbf{p} - \mathcal{B}^2\mathbf{p}) - \omega_n\big(\|\mathbf{p}\|^2_{\mathcal{S}} - 1\big)\mathbf{p},$$
$$\boldsymbol{D}_{\mathcal{S}} = \tfrac{1}{2}(\nabla_{\mathcal{S}}\mathbf{v} + (\nabla_{\mathcal{S}}\mathbf{v})^T), \quad \boldsymbol{\Omega}_{\mathcal{S}} = \tfrac{1}{2}(\nabla_{\mathcal{S}}\mathbf{v} - (\nabla_{\mathcal{S}}\mathbf{v})^T).$$

Besides the corresponding surface operators and the additional geometric coupling terms with the shape operator $\mathcal{B}$ and the mean curvature $\mathcal{H}$, we also obtain an explicit appearance of the normal velocity v_n in the director field equation. Overall the additional terms in the more general Ericksen-Leslie model lead to an even tighter coupling between geometric properties and dynamics. The described numerical approach, see Appendix A, can be adapted to also solve the surface active polar viscous gel model proposed in Eqs. (7)–(9). Figure 8 shows results on a torus. We use the same torus and the same initial conditions for the velocity field $\widehat{\mathbf{v}}$ and the director field $\widehat{\mathbf{p}}$ as considered in Fig. 2. The parameters are adapted to $\alpha = 1.1$, $\beta = 20$, $\lambda = 0.02$, $\nu = 200$, $\eta = 0.01$, and $\omega_n = 5$,

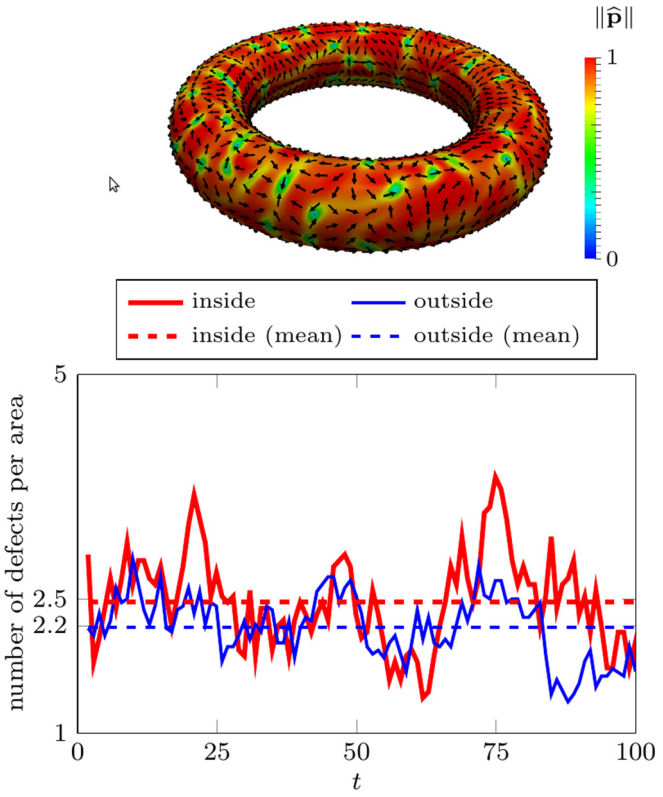

FIG. 8. Top: Snapshot of the director field $\widehat{\mathbf{p}}$ of the surface active polar viscous gel model on the torus for $t = 14.3$. Bottom: Number of defects per area for the inner ($\kappa < 0$) and the outer ($\kappa > 0$) region of the torus vs time t.

while all other parameters remain unchanged. Figure 8 (top) shows a snapshot of the director field; see also the video in the Supplemental Material [74]. The significantly reduced parameter η yields smeared out defects and promotes the annihilation and creation of new defects. In Fig. 8 (bottom) the number of defects per area against the time is plotted. Thereby, we distinguish between the inner ($\kappa < 0$) and the outer ($\kappa > 0$) region of the torus and observe slightly more defects per area in the inner part. This might be due to the stronger geometric force (resulting from a higher absolute value of the Gaussian curvature in the inner region), the continuous creation and annihilation of defects, as well as the fact that defects of opposite topological charge are attracted to each other. As in the passive case, a detailed analysis of such phenomena has to be discussed elsewhere.

ACKNOWLEDGMENTS

This work was financially supported by the German Research Foundation (DFG) through project Vo899-19. We used computing resources provided by Jülich Supercomputing Centre within project HDR06.

APPENDIX A: NUMERICS

To efficiently solve the surface Navier-Stokes equation in [51] a heavy assembly workload was avoided by applying $\boldsymbol{\nu}\times$ to Eq. (4) and considering the rotated velocity field $\widehat{\mathbf{w}} := \boldsymbol{\nu} \times \widehat{\mathbf{v}}$. Since only the $\mathrm{Rot}_S\,\mathrm{rot}_S\,(\cdot)$ operator occurs as second-order operator, we here can also use the same idea to

reduce the assembly costs. Thus, the rotated version of Eqs. (4) and (5) with tangential penalization of the rotated velocity $\widehat{\mathbf{w}}$ now reads

$$\pi_{\mathcal{S}}\partial_t\widehat{\mathbf{w}} + \nabla_{\widehat{\mathbf{w}}}\widehat{\mathbf{w}} = -\operatorname{rot}_{\mathcal{S}} p + \nu(\nabla_{\mathcal{S}}\operatorname{div}_{\mathcal{S}}\widehat{\mathbf{w}} + 2\kappa\widehat{\mathbf{w}}) + \mathbf{f}_g + \mathbf{f}_{\widehat{\mathbf{w}}} - \lambda\boldsymbol{\nu}\times\operatorname{div}_{\mathcal{S}}\widehat{\boldsymbol{\sigma}}^{\mathrm{E}}_{\mathcal{S}}, \tag{A1}$$

$$\operatorname{rot}_{\mathcal{S}}\widehat{\mathbf{w}} = v_n\mathcal{H}, \tag{A2}$$

where we used for convenience the abbreviations

$$\mathbf{f}_g := v_n\operatorname{rot}_{\mathcal{S}} v_n + 2\nu[\mathcal{H}\operatorname{rot}_{\mathcal{S}} v_n - \boldsymbol{\nu}\times(\mathcal{B}\nabla_{\mathcal{S}} v_n)],$$
$$\mathbf{f}_{\widehat{\mathbf{w}}} := -v_n\boldsymbol{\nu}\times[\mathcal{B}(\boldsymbol{\nu}\times\widehat{\mathbf{w}})] - \alpha_{\mathbf{v}}(\widehat{\mathbf{w}}\cdot\boldsymbol{\nu})\boldsymbol{\nu},$$

and the alternative form of the viscous terms proposed in (B23).

1. Time discretization

For the discretization in time we again use the same approach proposed in [51]. Let the time interval $[0, t_{\mathrm{end}}]$ be divided into a sequence of discrete times $0 < t^0 < t^1 < \cdots$ with time step width $\tau^m = t^m - t^{m-1}$. Thereby, the superscript denotes the time step number. The vector field $\widehat{\mathbf{w}}^m(\mathbf{x})$ correspond to the respective rotated velocity field $\widehat{\mathbf{w}}(\mathbf{x}, t^m)$. All other quantities follow the same notation. The time derivative is approximated by a standard difference quotient and a Chorin projection method [77] is applied to Eqs. (A1) and (A2). Furthermore, we define the discrete time derivatives $d^{\widehat{\mathbf{w}}}_{\tau^m} := \frac{1}{\tau^m}(\widehat{\mathbf{w}}^* - \pi_{\mathcal{S}}\widehat{\mathbf{w}}^{m-1})$ and $d^{\widehat{\mathbf{p}}}_{\tau^m} := \frac{1}{\tau^m}(\widehat{\mathbf{p}}^m - \pi_{\mathcal{S}}\widehat{\mathbf{p}}^{m-1})$, with $\pi_{\mathcal{S}}$ the projection to the surface at time t^m. Thus, we get a time-discrete version of Eqs. (A1), (A2), and (6)

$$d^{\widehat{\mathbf{w}}}_{\tau^m} + \nabla_{\widehat{\mathbf{w}}^{m-1}}\widehat{\mathbf{w}}^* = \nu(\nabla_{\mathcal{S}}\operatorname{div}_{\mathcal{S}}\widehat{\mathbf{w}}^* + 2\kappa\widehat{\mathbf{w}}^*) + \mathbf{f}_g + \mathbf{f}_{\widehat{\mathbf{w}}^*} - \lambda\boldsymbol{\nu}\times\operatorname{div}_{\mathcal{S}}\widehat{\boldsymbol{\sigma}}^{\mathrm{E}}_{\mathcal{S}}, \tag{A3}$$

$$\tau^m\Delta_{\mathcal{S}} p^m = \operatorname{rot}_{\mathcal{S}}\widehat{\mathbf{w}}^* - v_n\mathcal{H}, \tag{A4}$$

$$\widehat{\mathbf{w}}^m = \widehat{\mathbf{w}}^* - \tau^m\operatorname{rot}_{\mathcal{S}} p^m, \tag{A5}$$

$$d^{\widehat{\mathbf{p}}}_{\tau^m} + \nabla_{\widehat{\mathbf{v}}^m}\widehat{\mathbf{p}}^m = \eta(\widehat{\boldsymbol{\Delta}}^{\mathrm{DG}}\widehat{\mathbf{p}}^m - \mathcal{B}^2\widehat{\mathbf{p}}^m) - \omega_n(\|\widehat{\mathbf{p}}^{m-1}\|^2 - 1)\widehat{\mathbf{p}}^m - \alpha_{\mathbf{p}}(\boldsymbol{\nu}\cdot\widehat{\mathbf{p}}^m)\boldsymbol{\nu}, \tag{A6}$$

where $\widehat{\boldsymbol{\sigma}}^{\mathrm{E}}_{\mathcal{S}}$ is evaluated at the old time step, i.e., $\widehat{\boldsymbol{\sigma}}^{\mathrm{E}}_{\mathcal{S}} = (\nabla_{\mathcal{S}}\widehat{\mathbf{p}}^{m-1})^T\nabla_{\mathcal{S}}\widehat{\mathbf{p}}^{m-1} + (\mathcal{B}\widehat{\mathbf{p}}^{m-1})\otimes(\mathcal{B}\widehat{\mathbf{p}}^{m-1})$. Note that for readability we used a Taylor-0 linearization of the transport term in (A3) and the norm-1 penalization term in (6). In the simulations from above we performed a Taylor-1 linearization; see [26,50] for details.

2. Spatial discretization

The considered extension of the tangential vector fields to the Euclidean space allows us to apply the surface finite element method [64] for each component of the respective vector field. Let $\mathcal{S}_h$ denote the interpolation of the surface $\mathcal{S}(t^m)$ at time $t = t^m$ such that $\mathcal{S}_h := \bigcup_{T\in\mathcal{T}} T$ with a conforming triangulation $\mathcal{T}$. Furthermore, we introduce the finite element space

$$\mathbb{V}_h(\mathcal{S}_h) = \{v_h \in C^0(\mathcal{S}_h) \,:\, v_h|_T \in \mathbb{P}^1,\ \forall\, T \in \mathcal{T}\}$$

which is used twice as trail and test space and the standard L_2 scalar product on $\mathbb{V}_h(\mathcal{S}_h)$, $(\alpha, \beta) := \int_{\mathcal{S}_h}\langle\alpha, \beta\rangle d\mathcal{S}$. By using an operator splitting technique we decouple the hydrodynamic and the director field equation in the following way. First the surface finite element approximation of Eqs. (A3) and (A4) is solved, which reads as follows: find $\widehat{\mathbf{w}}^*_i$, $p^m \in \mathbb{V}_h(\mathcal{S}_h)$ s.t. $\forall\xi, \eta \in \mathbb{V}_h(\mathcal{S}_h)$

$$\big(\big(d^{\widehat{\mathbf{w}}}_{\tau^m}\big)_i + \nabla_{\widehat{\mathbf{w}}^{m-1}}\widehat{\mathbf{w}}^*_i - 2\nu\kappa\widehat{\mathbf{w}}^*_i - (\mathbf{f}_g + \mathbf{f}_{\widehat{\mathbf{w}}^*})_i, \xi\big) = -(\nu\operatorname{div}_{\mathcal{S}}\widehat{\mathbf{w}}^*, (\nabla_{\mathcal{S}}\xi)_i) - \big(\lambda\widehat{\boldsymbol{\sigma}}^{\mathrm{E}}_{\mathcal{S}}, \nabla_{\mathcal{S}}[\boldsymbol{\nu}\times(\xi\mathbf{e}_i)]\big),$$
$$(\tau^m\nabla_{\mathcal{S}} p^m, \nabla_{\mathcal{S}}\eta) = (v_n\mathcal{H} - \operatorname{rot}_{\mathcal{S}}\widehat{\mathbf{w}}^*, \eta)$$

for $i = x, y, z$. The resulting vector field $\widehat{\mathbf{w}}^*$ is then used to determine $\widehat{\mathbf{w}}^m$ by the pressure correction step in Eq. (A5). The transformation $\widehat{\mathbf{v}}^m = -\boldsymbol{\nu}\times\widehat{\mathbf{w}}^m$ leads to the velocity field at the new time step

t^m. Finally, the surface finite element approximation of Eq. (A6) is solved, which reads as follows: find $\widehat{\mathbf{p}}_i^m \in \mathbb{V}_h(\mathcal{S}_h)$ s.t. $\forall \xi \in \mathbb{V}_h(\mathcal{S}_h)$

$$\left(\left(d^{\widehat{\mathbf{p}}}_{\tau^m}\right)_i + \nabla_{\widehat{\mathbf{v}}^m}\widehat{\mathbf{p}}_i^m, \xi\right) = (\eta \nabla_{\mathcal{S}}\widehat{\mathbf{p}}^m, \nabla_{\mathcal{S}}(\xi\,\mathbf{e}_i)) - \left(\eta\mathcal{B}^2\widehat{\mathbf{p}}_i^m, \xi\right) - \left(\omega_n(\|\widehat{\mathbf{p}}^{m-1}\|^2 - 1)\widehat{\mathbf{p}}_i^m + \alpha_{\mathbf{p}}(\boldsymbol{\nu}\cdot\widehat{\mathbf{p}}^m)\boldsymbol{\nu}_i, \xi\right)$$

for $i = x, y, z$.

3. Pressure relaxation schemes

In some situations it is useful to modify the Chorin projection scheme (A3), (A4), and (A5). To be more precise the resulting finite element matrix of the pressure equation (A4) is sometimes ill-conditioned, especially when the term $\mathrm{rot}_{\mathcal{S}}\,\widehat{\mathbf{w}}^*$ is big compared to the others. The solution of Eq. (A4) can be seen as the steady-state solution of a heat conduction equation where the heat source is determined by the right-hand side of Eq. (A4). Therefore, we add a relaxation scheme in form of a discrete time derivative on a different timescale to the left-hand side of Eq. (A4), i.e.,

$$\tfrac{1}{\tau^*}(p^{m+1,l+1} - p^{m+1,l}) - \tau^m \Delta_{\mathcal{S}} p^{m+1,l+1} = -\,\mathrm{rot}_{\mathcal{S}}\,\widehat{\mathbf{w}}^* + v_n\mathcal{H}, \tag{A7}$$

where τ^* denotes the time step and l the time step number on the different timescale. Instead of solving Eq. (A4), the iterative process in Eq. (A7) is performed until a steady state is reached, which is then used in the correction step in Eq. (A5).

APPENDIX B: THIN FILM LIMIT

We assume a regular moving surface $\mathcal{S}(t) \subset \mathbb{R}^3$ without boundaries and a thin film $\Omega_h(t) := \mathcal{S}(t) \times [-h/2, h/2] \subset \mathbb{R}^3$ of sufficiently small thickness h, such that the thin film parametrization $\mathbf{X}(t, y^1, y^2, \xi) = \mathbf{x}(t, y^1, y^2) + \xi\,\boldsymbol{\nu}(t, y^1, y^2)$ is injective for the surface parametrization $\mathbf{x}(t, \cdot, \cdot)$. Thereby, y^1 and y^2 denote the local surface coordinates, $\boldsymbol{\nu}(t, \cdot, \cdot)$ is the surface normal field, and $\xi \in [-h/2, h/2]$ is the local normal coordinate. Since the thin film is moving according to the surface, the parametrization $\mathbf{X}$ is not unique, which arises from the choice of an observer within the thin film. For a pure Eulerian observer, i.e., for the observer velocity $\boldsymbol{W} = \partial_t\mathbf{X} = 0$, we are not able to formulate proper intrinsic physics at the surface $\mathcal{S}$ for $h \to 0$. To overcome this issue, we choose a transversal observer as the surface observer parametrization $\mathbf{x}$, i.e., Eulerian in the tangential space and Lagrangian in normal direction and hence $\partial_t\mathbf{x} = \partial_t\mathbf{X}|_{\mathcal{S}} = v_n\boldsymbol{\nu}$, where $v_n = W^{\xi}|_{\mathcal{S}}$ is the normal surface velocity of $\mathcal{S}$. To ensure a constant thickness h of the thin film and that the surface $\mathcal{S}$ is located in the middle of the thin film over time, we stipulating the same transversal behavior for both boundary surfaces. Thus, we get $\partial_t\mathbf{X}|_{\partial\Omega_h} = v_n\boldsymbol{\nu} \pm \frac{h}{2}\partial_t\boldsymbol{\nu} = W^{\xi}|_{\partial\Omega_h}\boldsymbol{\nu}$ and therefore $W^{\xi}|_{\partial\Omega_h} = v_n$, since $\partial_t\boldsymbol{\nu}$ is always tangential on the boundaries $\partial\Omega_h$.

For notational compactness of tensor algebra we use the thin film calculus presented in [27] and [26] (Appendix) which is based on Ricci calculus, where lowercase indices $i, j, k, \ldots$ denote components w.r.t. y^1 and y^2 in the surface coordinate system, and uppercase indices $I, J, K, \ldots$ denote components w.r.t. y^1, y^2, and ξ in the extended three-dimensional thin film coordinate system. Metric quantities at the surface $\mathcal{S}$ are the metric tensor $g_{ij} = \langle\partial_i\mathbf{x}, \partial_j\mathbf{x}\rangle_{\mathbb{R}^3}$ (first fundamental form), the shape operator $B_{ij} = -\langle\partial_i\mathbf{x}, \partial_j\boldsymbol{\nu}\rangle_{\mathbb{R}^3}$ (second fundamental form), its square $[\mathcal{B}^2]_{ij} = B_{ik}B^k_j = \langle\partial_i\boldsymbol{\nu}, \partial_j\boldsymbol{\nu}\rangle_{\mathbb{R}^3}$ (third fundamental form), the mean curvature $\mathcal{H} = \mathrm{tr}\,\mathcal{B} = B^i_i$, the Gaussian curvature $\kappa = \det\mathcal{B}^\sharp = \det\{B^{ij}\}$, and the Christoffel symbols $\Gamma^k_{ij} = \frac{1}{2}g^{kl}(\partial_i g_{jl} + \partial_j g_{il} - \partial_l g_{ij})$ for covariant differentiating (e.g., $[\nabla_{\mathcal{S}}\mathbf{p}]^i_k = p^i_{|k} = \partial_k p^i + \Gamma^i_{kj}p^j$ for a contravariant vector field $\mathbf{p} \in \mathsf{T}\mathcal{S} = \mathsf{T}^1\mathcal{S}$). In the thin film Ω_h, the metric tensor $G_{IJ} = \langle\partial_I\mathbf{X}, \partial_J\mathbf{X}\rangle_{\mathbb{R}^3}$ and the Christoffel symbols $\Gamma^K_{IJ} = \frac{1}{2}G^{KL}(\partial_I G_{JL} + \partial_J G_{IL} - \partial_L G_{IJ})$ for covariant differentiating (e.g., $[\nabla\boldsymbol{P}]^I_K = P^I_{;K} = \partial_K P^I + \Gamma^I_{KJ}P^J$ for a contravariant vector field $\boldsymbol{P} \in \mathsf{T}\Omega_h = \mathsf{T}^1\Omega_h$) can be developed at the surface by $G_{ij} = g_{ij} - 2\xi B_{ij} + \xi^2[\mathcal{B}^2]_{ij}$, $G_{\xi\xi} = 1$, $G_{\xi i} = G_{i\xi} = 0$, $G^{ij} = g^{ij} + \mathcal{O}(\xi)$, $G^{\xi\xi} = 1$, $G^{\xi i} = G^{i\xi} = 0$, $\Gamma^k_{ij} = \Gamma^k_{ij} + \mathcal{O}(\xi)$, $\Gamma^{\xi}_{ij} = B_{ij} + \mathcal{O}(\xi)$, $\Gamma^k_{i\xi} = \Gamma^k_{\xi i} = -B^k_i + \mathcal{O}(\xi)$ and $\Gamma^{\xi}_{I\xi} = \Gamma^{\xi}_{\xi I} = \Gamma^K_{\xi\xi} = 0$; see [27] and [26] for details.

Our starting point is the simplified local three-dimensional Ericksen-Leslie model [31], i.e.,

$$\partial_t \boldsymbol{V} + \boldsymbol{\nabla}_{\boldsymbol{U}} \boldsymbol{V} = -\nabla P_{\Omega_h} + \nu \boldsymbol{\Delta} \boldsymbol{V} - \lambda \operatorname{div} \boldsymbol{\sigma}^{\mathrm{E}}, \tag{B1}$$

$$\operatorname{div} \boldsymbol{V} = 0, \tag{B2}$$

$$\partial_t \boldsymbol{P} + \boldsymbol{\nabla}_{\boldsymbol{U}} \boldsymbol{P} = \eta \boldsymbol{\Delta} \boldsymbol{P} - \omega_n \big(\|\boldsymbol{P}\|^2_{\Omega_h} - 1 \big) \boldsymbol{P} \tag{B3}$$

in $\Omega_h \times \mathbb{R}_+$, with fluid velocity $\boldsymbol{V} \in \mathsf{T}\Omega_h$, relative fluid velocity $\boldsymbol{U} = \boldsymbol{V} - \boldsymbol{W} \in \mathsf{T}\Omega_h$ with respect to the observer velocity $\boldsymbol{W} = \partial_t \mathbf{X}$, director field $\boldsymbol{P} \in \mathsf{T}\Omega_h$, pressure P_{Ω_h}, Ericksen stress tensor $\boldsymbol{\sigma}^{\mathrm{E}} = (\nabla \boldsymbol{P})^T \nabla \boldsymbol{P}$, fluid viscosity ν, competition between kinetic and elastic potential energy λ, and elastic relaxation time for the molecular orientation field η. Besides initial conditions, we consider homogeneous Dirichlet boundary conditions for the normal components and Neumann boundary conditions for the tangential components of the director and homogeneous Navier boundary conditions for the velocity field, i.e.,

$$\langle \boldsymbol{P}, \boldsymbol{\nu} \rangle_{\Omega_h} = P_\xi = 0, \tag{B4}$$

$$\boldsymbol{\nabla}_{\boldsymbol{\nu}} \big(\pi^{\flat}_{\partial\Omega_h} \boldsymbol{P} \big)^{\flat} = \{ P_{i;\xi} \} = 0, \tag{B5}$$

$$\pi^{\flat}_{\partial\Omega_h} (\boldsymbol{\nu} \cdot \mathcal{L}_{\boldsymbol{V}} \boldsymbol{G}) = \{ V_{i;\xi} + V_{\xi;i} \} = 0 \tag{B6}$$

at the boundaries $\partial\Omega_h$ in its covariant form. Thereby, $\mathcal{L}_{\boldsymbol{V}} \boldsymbol{G}$ denotes the viscous stress tensor in terms of the Lie derivative $\mathcal{L}$ and $\pi^{\flat}_{\partial\Omega_h} : \mathsf{T}_1\Omega_h|_{\partial\Omega_h} \to \mathsf{T}_1 \partial\Omega_h$ is the orthogonal covariant projection into the covariant boundary tangential space. Note that it holds that

$$\langle \boldsymbol{V}, \boldsymbol{\nu} \rangle_{\Omega_h} = V_\xi = W_\xi = v_n$$

on $\partial\Omega_h$, which follows from the special choice of the transversal observer from above.

As proposed in [27] the boundary quantities are continuable to the surface $\mathcal{S}$ by Taylor expansions at the boundaries, which, e.g., results in

$$P_\xi|_{\mathcal{S}} = \mathcal{O}(h^2), \quad P_{\xi;\xi}|_{\mathcal{S}} = \mathcal{O}\big(h^2\big), \tag{B7}$$

$$P_{i;\xi}|_{\mathcal{S}} = \mathcal{O}(h^2), \quad P_{i;\xi;\xi}|_{\mathcal{S}} = \mathcal{O}(h^2), \tag{B8}$$

$$V_{\xi;\xi}|_{\mathcal{S}} = \mathcal{O}(h^2), \quad V_{\xi;\xi;\xi}|_{\mathcal{S}} = \mathcal{O}(h^2), \tag{B9}$$

$$V_{i;\xi}|_{\mathcal{S}} + V_{\xi;i}|_{\mathcal{S}} = \mathcal{O}(h^2), \tag{B10}$$

$$V_{i;\xi;\xi}|_{\mathcal{S}} + V_{\xi;i;\xi}|_{\mathcal{S}} = \mathcal{O}(h^2). \tag{B11}$$

Note that the right identity of Eq. (B9) is achieved by using $V_\xi|_{\mathbf{X}(\xi=-\frac{h}{2})} = V_\xi|_{\mathbf{X}(\xi=\frac{h}{2})} = V_\xi|_{\mathbf{X}(\xi=0)} = v_n$, the related second-order difference quotient, and $V_{\xi;\xi;\xi} = \partial^2_\xi V_\xi$. The latter follows due to the fact that the Christoffel symbols $\mathbb{\Gamma}^K_{\xi\xi}$ vanish identically.

With all these tools from above, we are able to realize a thin film limit of Eqs. (B1)–(B3) for $h \to 0$, consistently, by Taylor expansion of the equations at the surface. The thin film Ω_h is a flat Riemannian manifold and therefore the Riemannian curvature tensor vanishes, i.e., covariant derivatives commute, and with the continuity equation (B2) we obtain

$$[\boldsymbol{\Delta} \boldsymbol{V}]_I = [\operatorname{div} \nabla \boldsymbol{V} + \nabla \operatorname{div} \boldsymbol{V}]_I = V_I{}^{;K}{}_{;K} + V^K{}_{;K;I} = V_I{}^{;K}{}_{;K} + V^K{}_{;I;K} = [\operatorname{div} \mathcal{L}_{\boldsymbol{V}} \boldsymbol{G}]_I. \tag{B12}$$

Hence, we have to develop three divergence terms of 2-tensors at the surface in Eqs. (B1)–(B3), namely $\operatorname{div} \boldsymbol{T}|_{\mathcal{S}}$ for $\boldsymbol{T}$ being either $\mathcal{L}_{\boldsymbol{V}} \boldsymbol{G}$, $\boldsymbol{\sigma}^{\mathrm{E}}$, or $\nabla \boldsymbol{P}$. By using eqs. (B7)–(B11) it holds that

$$T_{i\xi}|_{\mathcal{S}} = \mathcal{O}(h^2), \quad \partial_\xi T_{i\xi}|_{\mathcal{S}} = \mathcal{O}(h^2), \quad T_{i\xi;\xi}|_{\mathcal{S}} = \mathcal{O}(h^2). \tag{B13}$$

The covariant tangential components of the divergence at the surface are

$$[\operatorname{div} \boldsymbol{T}]_i|_{\mathcal{S}} = T_i{}^K{}_{;K}\big|_{\mathcal{S}} = \big(\partial_K T_i{}^K - \mathbb{\Gamma}^J_{Ki} T_J{}^K + \mathbb{\Gamma}^K_{KL} T_i{}^L \big)\big|_{\mathcal{S}},$$

where it holds by using Eq. (B13) that

$$\partial_K T_i^K\big|_{\mathcal{S}} = \partial_k T_i^k\big|_{\mathcal{S}} + \mathcal{O}(h^2), \tag{B14}$$

$$\mathbb{\Gamma}^J_{Ki} T_J^K\big|_{\mathcal{S}} = \big(\Gamma^j_{ki} T_j^k + B_{ik} T_\xi^k\big)\big|_{\mathcal{S}} + \mathcal{O}(h^2), \tag{B15}$$

$$\mathbb{\Gamma}^K_{KL} T_i^L\big|_{\mathcal{S}} = \Gamma^k_{kl} T_i^l\big|_{\mathcal{S}} + \mathcal{O}(h^2). \tag{B16}$$

Adding this up and taking the metric compatibility of $\nabla_{\mathcal{S}}$ into account, we obtain

$$[\operatorname{div} \boldsymbol{T}]_i|_{\mathcal{S}} = \big(T_i^k\big|_{\mathcal{S}}\big)_{|k} - B_{ik} T_\xi^k\big|_{\mathcal{S}} + \mathcal{O}(h^2) = g^{kl}((T_{il}|_{\mathcal{S}})_{|k} - B_{ik} T_{\xi l}|_{\mathcal{S}}) + \mathcal{O}(h^2). \tag{B17}$$

Note that all normal derivatives vanished here, i.e., there is no need for a higher order expansion in ξ of the thin film Christoffel symbols as a consequence of the used boundary conditions. To substantiate the tensor $\boldsymbol{T} \in \mathsf{T}^{(2)}\Omega_h$, we first observe that

$$V_{i;j}|_{\mathcal{S}} = \big(\partial_j V_i - \mathbb{\Gamma}^k_{ji} V_k - \mathbb{\Gamma}^\xi_{ji} V_\xi\big)\big|_{\mathcal{S}} = v_{i|j} - v_n B_{ij}, \tag{B18}$$

$$P_{i;j}|_{\mathcal{S}} = \big(\partial_j P_i - \mathbb{\Gamma}^k_{ji} P_k - \mathbb{\Gamma}^\xi_{ji} P_\xi\big)\big|_{\mathcal{S}} = p_{i|j} + \mathcal{O}(h^2), \tag{B19}$$

$$P_{\xi;j}|_{\mathcal{S}} = \big(\partial_j P_\xi - \mathbb{\Gamma}^k_{j\xi} P_k\big)\big|_{\mathcal{S}} = B_j{}^k p_k + \mathcal{O}(h^2), \tag{B20}$$

where $v_i := V_i|_{\mathcal{S}}$ and $p_i := P_i|_{\mathcal{S}}$, i.e., $\mathbf{v} := \pi_{\mathcal{S}} \boldsymbol{V}|_{\mathcal{S}} \in \mathsf{T}^1\mathcal{S}$ and in contravariant form $\mathbf{p} := \pi_{\mathcal{S}} \boldsymbol{P}|_{\mathcal{S}} \in \mathsf{T}^1\mathcal{S}$. We further obtain

$$\begin{aligned}
[\mathcal{L}_{\boldsymbol{V}} \boldsymbol{G}]_{il}|_{\mathcal{S}} &= v_{i|l} + v_{l|i} - 2 v_n B_{il} = [\mathcal{L}_{\mathbf{v}} \boldsymbol{g} - 2 v_n B]_{il}, \\
[\boldsymbol{\sigma}^{\mathrm{E}}]_{il}\big|_{\mathcal{S}} &= [(\nabla \boldsymbol{P})^T \nabla \boldsymbol{P}]_{il}\big|_{\mathcal{S}} = (G^{jk} p_{j;i} p_{k;l} + p_{\xi;i} p_{\xi;l})\big|_{\mathcal{S}} \\
&= [(\nabla_{\mathcal{S}} \mathbf{p})^T \nabla_{\mathcal{S}} \mathbf{p} + (\mathcal{B}\mathbf{p}) \otimes (\mathcal{B}\mathbf{p})]_{il} + \mathcal{O}(h^2),
\end{aligned}$$

which we define as the extrinsic surface Ericksen stress tensor $\boldsymbol{\sigma}^{\mathrm{E}}_{\mathcal{S}} := (\nabla_{\mathcal{S}} \mathbf{p})^T \nabla_{\mathcal{S}} \mathbf{p} + (\mathcal{B}\mathbf{p}) \otimes (\mathcal{B}\mathbf{p})$, and finally get

$$\begin{aligned}
\pi_{\mathcal{S}}(\boldsymbol{\Delta} \boldsymbol{V})|_{\mathcal{S}} &= \operatorname{div}_{\mathcal{S}} (\mathcal{L}_{\mathbf{v}} \boldsymbol{g} - 2 v_n B) + \mathcal{O}(h^2), \\
\pi_{\mathcal{S}}(\boldsymbol{\Delta} \boldsymbol{P})|_{\mathcal{S}} &= \boldsymbol{\Delta}^{\mathrm{DG}} \mathbf{p} - \mathcal{B}^2 \mathbf{p} + \mathcal{O}(h^2), \\
\pi_{\mathcal{S}} \operatorname{div} \boldsymbol{\sigma}^{\mathrm{E}}|_{\mathcal{S}} &= \operatorname{div}_{\mathcal{S}} \boldsymbol{\sigma}^{\mathrm{E}}_{\mathcal{S}} + \mathcal{O}(h^2),
\end{aligned} \tag{B21}$$

where Eq. (B17) was used and $\boldsymbol{\Delta}^{\mathrm{DG}} := \operatorname{div}_{\mathcal{S}} \circ \nabla_{\mathcal{S}}$ denotes the Bochner Laplacian. Evaluating Eq. (B2) at the surface and using the boundary condition (B9) and the identity in Eq. (B18) gives

$$0 = \operatorname{div} \boldsymbol{V}|_{\mathcal{S}} = (G^{ij} V_{i;j} + V_{\xi;\xi})|_{\mathcal{S}} = \operatorname{div}_{\mathcal{S}} \mathbf{v} - v_n \mathcal{H} + \mathcal{O}(h^2). \tag{B22}$$

Furthermore, we introduce the two curl operators $\operatorname{rot}_{\mathcal{S}} : \mathsf{T}^{(1)}\mathcal{S} \to \mathsf{T}^0\mathcal{S}$ for vector fields and $\operatorname{Rot}_{\mathcal{S}} : \mathsf{T}^0\mathcal{S} \to \mathsf{T}^{(1)}\mathcal{S}$ for scalar fields; see [26,50] for their definitions. Therefore, rewriting Eq. (B21) yields

$$\begin{aligned}
\pi_{\mathcal{S}}(\boldsymbol{\Delta} \boldsymbol{V})|_{\mathcal{S}} &= \operatorname{Rot}_{\mathcal{S}} \operatorname{rot}_{\mathcal{S}} \mathbf{v} + 2(\kappa \mathbf{v} + \mathcal{H} \nabla_{\mathcal{S}} v_n) - 2\mathcal{B} \nabla_{\mathcal{S}} v_n + \mathcal{O}(h^2) \\
&= -\boldsymbol{\Delta}^{\mathrm{dR}} \mathbf{v} + 2\kappa \mathbf{v} + \nabla_{\mathcal{S}}(v_n \mathcal{H}) - 2 \operatorname{div}_{\mathcal{S}} (v_n \mathcal{B}) + \mathcal{O}(h^2),
\end{aligned} \tag{B23}$$

as a consequence of Eq. (B22) and the Weizenböck machinery, i.e., interchanging covariant derivatives w.r.t. the Riemannian curvature tensor of $\mathcal{S}$; cf. [48]. With

$$\|\boldsymbol{P}\|^2_{\Omega_h}\big|_{\mathcal{S}} = (G^{ij} P_i P_j + (P_\xi)^2)|_{\mathcal{S}} = \|\mathbf{p}\|^2_{\mathcal{S}} + \mathcal{O}(h^4)$$

we get for the remaining terms on the right-hand sides of Eqs. (B3) and (B1)

$$\pi_{\mathcal{S}}\big((\|\boldsymbol{P}\|^2_{\Omega_h} - 1)\boldsymbol{P}\big)\big|_{\mathcal{S}} = \big(\|\mathbf{p}\|^2_{\mathcal{S}} - 1\big)\mathbf{p} + \mathcal{O}(h^4), \quad \pi_{\mathcal{S}}(\nabla P_{\Omega_h})\big|_{\mathcal{S}} = \nabla_{\mathcal{S}} p_{\mathcal{S}},$$

with the surface pressure $p_{\mathcal{S}} := P_{\Omega_h}|_{\mathcal{S}}$. Note that it holds for the relative velocity at the surface $\boldsymbol{U}|_{\mathcal{S}} = \pi_{\mathcal{S}} \boldsymbol{V}|_{\mathcal{S}}$, i.e., $U_\xi|_{\mathcal{S}} = 0$ and $U^i|_{\mathcal{S}} = v^i$, on the left-hand sides of Eqs. (B1) and (B3). Hence,

Eqs. (B18) and (B19) now read

$$[\nabla_{\boldsymbol{U}}\boldsymbol{V}]_i|_{\mathcal{S}} = v^k V_{i;k}|_{\mathcal{S}} = \big[\nabla^{\mathcal{S}}_{\mathbf{v}}\mathbf{v} - v_n\mathcal{B}\mathbf{v}\big]_i, \quad [\nabla_{\boldsymbol{U}}\boldsymbol{P}]_i\big|_{\mathcal{S}} = v^k P_{i;k}\big|_{\mathcal{S}} = \big[\nabla^{\mathcal{S}}_{\mathbf{v}}\mathbf{p}\big]_i + \mathcal{O}(h^2).$$

By using $\partial_t\mathbf{X} = \boldsymbol{W} = W_\xi\boldsymbol{\nu}$, $W_\xi|_{\mathcal{S}} = v_n$, and $\boldsymbol{V} = V^k\partial_k\mathbf{X} + V_\xi\boldsymbol{\nu}$ (analogously for $\boldsymbol{P}$) we obtain for the partial time derivatives

$$\begin{aligned}[\partial_t\boldsymbol{V}]_i\big|_{\mathcal{S}} &= \langle\partial_t\boldsymbol{V}, \partial_i\mathbf{X}\rangle_{\Omega_h}\big|_{\mathcal{S}} = \langle(\partial_t V^k)\partial_k\mathbf{X} + V^k\partial_k\boldsymbol{W} + (\partial_t V_\xi)\boldsymbol{\nu} + V_\xi\partial_t\boldsymbol{\nu}, \partial_i\mathbf{X}\rangle_{\Omega_h}\big|_{\mathcal{S}} \\ &= g_{ik}\partial_t v^k + v^k\langle(\partial_k W_\xi)\boldsymbol{\nu} + v_n\partial_k\boldsymbol{\nu}, \partial_i\mathbf{X}\rangle_{\Omega_h}\big|_{\mathcal{S}} - v_n\langle\boldsymbol{\nu}, \partial_i\boldsymbol{W}\rangle_{\Omega_h}\big|_{\mathcal{S}} \\ &= g_{ik}\partial_t v^k - v_n(B_{ik}v^k + \partial_i v_n) \end{aligned} \tag{B24}$$

and

$$\begin{aligned}[\partial_t\boldsymbol{P}]_i|_{\mathcal{S}} &= \langle\partial_t\boldsymbol{P}, \partial_i\mathbf{X}\rangle_{\Omega_h}\big|_{\mathcal{S}} = \big\langle\big(\partial_t P^k\big)\partial_k\mathbf{X} + P^k\partial_k\boldsymbol{W}, \partial_i\mathbf{X}\big\rangle_{\Omega_h}\big|_{\mathcal{S}} + \mathcal{O}(h^2) \\ &= g_{ik}\partial_t p^k - v_n B_{ik}p^k + \mathcal{O}(h^2). \end{aligned} \tag{B25}$$

Therefore, we have

$$\pi_{\mathcal{S}}[\partial_t\boldsymbol{V} + \nabla_{\boldsymbol{U}}\boldsymbol{V}]\big|_{\mathcal{S}} = (\partial_t\mathbf{v}^i)\partial_i\mathbf{x} + \nabla^{\mathcal{S}}_{\mathbf{v}}\mathbf{v} - v_n(2\mathcal{B}\mathbf{v} + \nabla_{\mathcal{S}}v_n) \tag{B26}$$

for the tangential part of the fluid acceleration in Eq. (B1). The same term was proposed in [42] by variation of the kinetic energy of a moving manifold in the context of Lagrangian field theory. Moreover, we also find this acceleration term in [45], where a covariant material derivative is derived in terms of covariant tensor transport through a three-dimensional moving spacetime embedded in a four-dimensional absolute space. In this context Eq. (B26) can be obtained by taking the spatial part of the covariant material derivative for the special case of velocity fields and a transversal observer. Evaluating the transport term for the director field $\boldsymbol{P}$ at the surface yields

$$\pi_{\mathcal{S}}[\partial_t\boldsymbol{P} + \nabla_{\boldsymbol{U}}\boldsymbol{P}]\big|_{\mathcal{S}} = (\partial_t\mathbf{p}^i)\partial_i\mathbf{x} + \nabla^{\mathcal{S}}_{\mathbf{v}}\mathbf{p} - v_n B\mathbf{p},$$

which can also be found in [45], but as the spatial part of the covariant material derivative of a so-called instantaneous vector field from a point of view of a transversal observer. Finally, under boundary conditions (B4)–(B6) and $h \to 0$, Eq. (B2) and the tangential parts of Eqs. (B1) and (B3) reduce to

$$\begin{aligned}(\partial_t\mathbf{v}^i)\partial_i\mathbf{x} + \nabla^{\mathcal{S}}_{\mathbf{v}}\mathbf{v} - v_n(2\mathcal{B}\mathbf{v} + \nabla_{\mathcal{S}}v_n) = -\nabla_{\mathcal{S}}p_{\mathcal{S}} + \nu(-\boldsymbol{\Delta}^{\mathrm{dR}}\mathbf{v} + 2\kappa\mathbf{v} + \nabla_{\mathcal{S}}(v_n\mathcal{H}) - 2\,\mathrm{div}_{\mathcal{S}}\,(v_n\mathcal{B})) \\ - \lambda\,\mathrm{div}_{\mathcal{S}}\,\boldsymbol{\sigma}^{\mathrm{E}}_{\mathcal{S}}, \end{aligned} \tag{B27}$$

$$\mathrm{div}_{\mathcal{S}}\,\mathbf{v} = v_n\mathcal{H}, \tag{B28}$$

$$(\partial_t\mathbf{p}^i)\partial_i\mathbf{x} + \nabla^{\mathcal{S}}_{\mathbf{v}}\mathbf{p} - v_n B\mathbf{p} = \eta(\boldsymbol{\Delta}^{\mathrm{DG}}\mathbf{p} - \mathcal{B}^2\mathbf{p}) - \omega_n\big(\|\mathbf{p}\|^2_{\mathcal{S}} - 1\big)\mathbf{p} \tag{B29}$$

in $\mathcal{S}\times\mathbb{R}_+$. This system of PDEs has full rank, i.e., it contains five independent coupled equations with five degrees of freedom v^1, v^2, p^1, p^2, depending on an arbitrary choice of local coordinates, and $p_{\mathcal{S}}$. A full discussion about the normal parts of Eqs. (B1) and (B3) does not belong to this paper. Nevertheless, the normal parts would give us two additional equations, consistently w.r.t. h, and two new free scalar valued quantities $\gamma_1, \gamma_2 \in \mathsf{T}^0\mathcal{S}$. With our boundary conditions and assumption, w.r.t. the moving thin film geometry, this would be $\gamma_1 := \partial_\xi P_{\Omega_h}|_{\mathcal{S}}$ and $\gamma_2 := P_{\xi;\xi;\xi}|_{\mathcal{S}} = \partial^2_\xi P_\xi|_{\mathcal{S}}$. Both degrees of freedom would occur as zero-order differential terms, i.e., the upcoming normal equations would not have any influence on Eqs. (B27)–(B29). Therefore, the thin film limit of the normal part equations can be omitted as long as we are not interested in the quantities γ_1 and γ_2.

The partial time derivatives in Eqs. (B27) and (B29) are realized only at the contravariant vector proxies of $\mathbf{v}$ and $\mathbf{p}$ w.r.t. locally defined charts at the surface. The reason for the absence of an intrinsic covariant vector operator notation for the time derivative (similar to $\nabla_{\mathcal{S}}$) is that the time t is not a coordinate of a moving space in a pure spatial perspective, especially for a moving surface with $v_n \neq 0$. Unfortunately, most of the numerical tools for solving surface PDEs do not work with

a locally defined vector basis. They mimic vector-valued problems as a system of scalar-valued problems under the assumption of Euclidean coordinates. This means for the surface problem (B27)–(B29) that the tangential velocity field and the director field are considered to be vector fields in $\mathbb{R}^3$, which results in an underdetermined problem. The two additional degrees of freedom can be handled in different ways, e.g., by penalty methods [26,51] or by using Lagrange multipliers [43]. The terms $\partial_t \mathbf{v}$ and $\partial_t \mathbf{p}$ certainly makes sense, if we consider $\mathbf{v}$, $\mathbf{p} \in \mathsf{T}\mathbb{R}^3$, but note that in general $\partial_t \mathbf{v}$ as well as $\partial_t \mathbf{p}$ are no longer part of the tangential space of the surface $\mathcal{S}$. Nevertheless, we can use only the tangential part of $\partial_t \mathbf{v} = (\partial_t v^j)\partial_j \mathbf{x} + v^j \partial_j \partial_t \mathbf{x}$ for a transversal observer, i.e.,

$$[\partial_t \mathbf{v}]_i = \langle \partial_t \mathbf{v}, \partial_i \mathbf{x} \rangle_{\mathbb{R}^3} = g_{ij} \partial_t v^j - v_n B_{ij} v^j.$$

Analogously, the same holds for $\partial_t \mathbf{p}$. Finally, we obtain by rewriting Eqs. (B27)–(B29),

$$\pi_{\mathcal{S}} \partial_t \mathbf{v} + \nabla^{\mathcal{S}}_{\mathbf{v}} \mathbf{v} - v_n(\mathcal{B}\mathbf{v} + \nabla_{\mathcal{S}} v_n) = -\nabla_{\mathcal{S}} p_{\mathcal{S}} + \nu(-\boldsymbol{\Delta}^{\mathrm{dR}}\mathbf{v} + 2\kappa \mathbf{v} + \nabla_{\mathcal{S}}(v_n \mathcal{H}) - 2\,\mathrm{div}_{\mathcal{S}}\,(v_n \mathcal{B})) - \lambda\,\mathrm{div}_{\mathcal{S}}\,\boldsymbol{\sigma}^{\mathrm{E}}_{\mathcal{S}}, \tag{B30}$$

$$\mathrm{div}_{\mathcal{S}}\,\mathbf{v} = v_n \mathcal{H}, \tag{B31}$$

$$\pi_{\mathcal{S}} \partial_t \mathbf{p} + \nabla^{\mathcal{S}}_{\mathbf{v}} \mathbf{p} = \eta(\boldsymbol{\Delta}^{\mathrm{DG}}\mathbf{p} - \mathcal{B}^2 \mathbf{p}) - \omega_n\big(\|\mathbf{p}\|^2_{\mathcal{S}} - 1\big)\mathbf{p}, \tag{B32}$$

in $\mathcal{S} \times \mathbb{R}_+$, if $\mathbf{v}$, $\mathbf{p} \in \mathsf{T}\mathcal{S} \subset \mathsf{T}\mathbb{R}^3$.

Equation (B3) together with the boundary condition (B5) is the L_2-gradient flow along the material motion to minimize the Frank-Oseen energy functional with material constants $\eta = K_{11} = K_{22} = K_{33}$ and $K_{24} = 0$; see [78]. In the thin film limit, this leads to the minimization of the surface Frank-Oseen energy $\frac{\eta}{2}\int_{\mathcal{S}} \|\nabla_{\mathcal{S}} \mathbf{p}\|^2_{\mathcal{S}} d\mathcal{S}$. This situation differs from [26], where the one-constant approximation $\eta = K_{11} = K_{22} = K_{33} = -K_{24}$ was assumed, which leads to minimizing the distortion energy $\frac{\eta}{2}\int_{\mathcal{S}} (\mathrm{rot}_{\mathcal{S}}\,\mathbf{p})^2 + (\mathrm{div}_{\mathcal{S}}\,\mathbf{p})^2 d\mathcal{S}$. However, for the case $\omega_n \to \infty$, where $\|\mathbf{p}\|^2_{\mathcal{S}} = 1$ a. e., both energies only differ by a constant value $\frac{K}{2}\int_{\mathcal{S}} \kappa d\mathcal{S} = \pi K \chi(\mathcal{S})$, where $\chi(\mathcal{S})$ denotes the Euler characteristic. Thus, the minimizers of both energies are equal.

[1] P. G. de Gennes and J. Prost, *The Physics of Liquid Crystals*, 2nd ed. (Oxford University Press, Oxford, 1993).

[2] P. M. Chaikin and T. C. Lubensky, *Principles of Condensed Matter Physics* (Cambridge University Press, Cambridge, 1995).

[3] J. Dzubiella, M. Schmidt, and H. Löwen, Topological defects in nematic droplets of hard spherocylinders, Phys. Rev. E **62**, 5081 (2000).

[4] M. A. Bates, G. Skačej, and C. Zannoni, Defects and ordering in nematic coatings on uniaxial and biaxial colloids, Soft Matter **6**, 655 (2010).

[5] H. Shin, M. J. Bowick, and X. Xing, Topological Defects in Spherical Nematics, Phys. Rev. Lett. **101**, 037802 (2008).

[6] S. Dhakal, F. J. Solis, and M. Olvera de la Cruz, Nematic liquid crystals on spherical surfaces: Control of defect configurations by temperature, density, and rod shape, Phys. Rev. E **86**, 011709 (2012).

[7] V. Koning, T. Lopez-Leon, A. Fernández-Nieves, and V. Vitelli, Bivalent defect configurations in inhomogeneous nematic shells, Soft Matter **9**, 4993 (2013).

[8] G. Napoli and L. Vergori, Extrinsic Curvature Effects on Nematic Shells, Phys. Rev. Lett. **108**, 207803 (2012).

[9] H. Stark, Physics of colloidal dispersions in nematic liquid crystals, Phys. Rep. **351**, 387 (2001).

[10] P. Prinsen and P. van der Schoot, Shape and director-field transformation of tactoids, Phys. Rev. E **68**, 021701 (2003).

[11] A. Martinez, M. Ravnik, B. Lucero, R. Visvanathan, S. Zumer, and I. I. Smalyukh, Mutually tangled colloidal knots and induced defect loops in nematic fields, Nat. Mater. **13**, 258 (2014).

[12] A. Fernández-Nieves, V. Vitelli, A. S. Utada, D. R. Link, M. Márquez, D. R. Nelson, and D. A. Weitz, Novel Defect Structures in Nematic Liquid Crystal Shells, Phys. Rev. Lett. **99**, 157801 (2007).
[13] T. Lopez-Leon, A. Fernández-Nieves, M. Nobili, and C. Blanc, Smectic shells, J. Phys.: Condens. Matter **24**, 284122 (2012).
[14] H.-L. Liang, J. H. Noh, R. Zentel, P. Rudquist, and J. Lagerwall, Tuning the defect configurations in nematic and smectic liquid crystalline shells, Philos. Trans. R. Soc. London A **371** (2013).
[15] H. L. Liang, S. Schymura, P. Rudquist, and J. Lagerwall, Nematic-Smectic Transition under Confinement in Liquid Crystalline Colloidal Shells, Phys. Rev. Lett. **106**, 247801 (2011).
[16] W. Zhou, J. Cao, W. Liu, and S. Stoyanov, How rigid rods self-assemble at curved surfaces, Angew. Chem., Int. Ed. Engl. **48**, 378 (2008).
[17] R. E.Guerra, C. P. Kelleher, A. D. Hollingsworth, and P. M. Chaikin, Freezing on a sphere, Nature (London) **554**, 346 (2018).
[18] I. B. Liu, N. Sharifi-Mood, and K. J. Stebe, Capillary assembly of colloids: Interactions on planar and curved interfaces, Annu. Rev. Condens. Matter Phys. **9**, 283 (2018).
[19] Z. Yang, J. Wei, Y. I. Sobolev, and B. A. Grzybowski, Systems of mechanized and reactive droplets powered by multi-responsive surfactants, Nature (London) **553**, 313 (2018).
[20] N. D. Bade, R. Kamien, R. Assoian, and K. Stebe, Patterned cell alignment in response to macroscale curvature, Biophys. J. **112**, 536a (2017).
[21] F. C. Keber, E. Loiseau, T. Sanchez, S. J. DeCamp, L. Giomi, M. J. Bowick, M. C. Marchetti, Z. Dogic, and A. R. Bausch, Topology and dynamics of active nematic vesicles, Science **345**, 1135 (2014).
[22] P. W. Ellis, D. J. G. Pearce, Y.-W. Chang, G. Goldsztein, L. Giomi, and A. Fernández-Nieves, Curvature-induced defect unbinding and dynamics in active nematic toroids, Nat. Phys. **14**, 85 (2018).
[23] T. C. Lubensky and J. Prost, Orientational order and vesicle shape, J. Phys. II **2**, 371 (1992).
[24] D. R. Nelson, Toward a tetravalent chemistry of colloids, Nano Lett. **2**, 1125 (2002).
[25] S. Kralj, R. Rosso, and E. G. Virga, Curvature control of valence on nematic shells, Soft Matter **7**, 670 (2011).
[26] M. Nestler, I. Nitschke, S. Praetorius, and A. Voigt, Orientational order on surfaces: The coupling of topology, geometry, and dynamics, J. Nonlinear Sci. **28**, 147 (2018).
[27] I. Nitschke, M. Nestler, S. Praetorius, H. Löwen, and A. Voigt, Nematic liquid crystals on curved surfaces: A thin film limit, Proc. R. Soc. London A **474**, 20170686 (2018).
[28] F. Alaimo, C. Köhler, and A. Voigt, Curvature controlled defect dynamics in topological active nematics, Sci. Rep. **7**, 5211 (2017).
[29] R. Sknepnek and S. Henkes, Active swarms on a sphere, Phys. Rev. E **91**, 022306 (2015).
[30] G. Napoli and L. Vergori, Hydrodynamic theory for nematic shells: The interplay among curvature, flow, and alignment, Phys. Rev. E **94**, 020701 (2016).
[31] F.-H. Lin and C. Liu, Existence of solutions for the Ericksen-Leslie system, Arch. Ration. Mech. Anal. **154**, 135 (2000).
[32] R. A. Simha and S. Ramaswamy, Hydrodynamic Fluctuations and Instabilities in Ordered Suspensions of Self-Propelled Particles, Phys. Rev. Lett. **89**, 058101 (2002).
[33] K. Kruse, J. F. Joanny, F. Jülicher, J. Prost, and K. Sekimoto, Asters, Vortices, and Rotating Spirals in Active Gels of Polar Filaments, Phys. Rev. Lett. **92**, 078101 (2004).
[34] J. L. Ericksen, Conservation laws for liquid crystals, T. Soc. Rheol. **5**, 23 (1961).
[35] J. L. Ericksen, Equilibrium theory of liquid crystals, in *Advances in Liquid Crystals*, edited by G. H. Brown (Elsevier, Amsterdam, 1976), pp. 233–298.
[36] F. M. Leslie, Some constitutive equations for liquid crystals, Arch. Ration. Mech. Anal. **28**, 265 (1968).
[37] F. Lin, J. Lin, and C. Wang, Liquid crystal flows in two dimensions, Arch. Ration. Mech. An. **197**, 297 (2010).
[38] X. Hu and H. Wu, Long-time dynamics of the nonhomogeneous incompressible flow of nematic liquid crystals, Commun. Math. Sci. **11**, 779 (2013).
[39] W. Wang, P. Zhang, and Z. Zhang, Well-posedness of the Ericksen–Leslie system, Arch. Ration. Mech. Anal. **210**, 837 (2013).

[40] J. Huang, F. Lin, and C. Wang, Regularity and existence of global solutions to the Ericksen–Leslie system in $\mathbb{R}^2$, Commun. Math. Phys. **331**, 805 (2014).
[41] S. Reuther and A. Voigt, The interplay of curvature and vortices in flow on curved surfaces, Multiscale Model. Simul. **13**, 632 (2015).
[42] A. Yavari, A. Ozakin, and S. Sadik, Nonlinear elasticity in a deforming ambient space, J. Nonlinear Sci. **26**, 1651 (2016).
[43] T. Jankuhn, M. A. Olshanskii, and A. Reusken, Incompressible fluid problems on embedded surfaces: Modeling and variational formulations, Interfaces Free Bound. **20**, 353 (2018).
[44] T.-H. Miura, On singular limit equations for incompressible fluids in moving thin domains, Quart. Appl. Math. **76**, 215 (2018).
[45] I. Nitschke and A. Voigt (unpublished).
[46] D. G. Ebin and J. Marsden, Groups of diffeomorphisms and the motion of an incompressible fluid, Ann. Math. **92**, 102 (1970).
[47] M. Mitrea and M. Taylor, Navier-Stokes equations on Lipschitz domains in Riemannian manifolds, Math. Ann. **321**, 955 (2001).
[48] M. Arroyo and A. DeSimone, Relaxation dynamics of fluid membranes, Phys. Rev. E **79**, 031915 (2009).
[49] I. Nitschke, A. Voigt, and J. Wensch, A finite element approach to incompressible two-phase flow on manifolds, J. Fluid Mech. **708**, 418 (2012).
[50] I. Nitschke, S. Reuther, and A. Voigt, Discrete Exterior Calculus (EC) for the Surface Navier-Stokes Equation, in *Transport Processes at Fluidic Interfaces*, edited by D. Bothe and A. Reusken (Springer, Berlin, 2017), pp. 177–197.
[51] S. Reuther and A. Voigt, Solving the incompressible surface Navier-Stokes equation by surface finite elements, Phys. Fluids **30**, 012107 (2018).
[52] R. Abraham, J. E. Marsden, and T. S. Ratiu, *Manifolds, Tensor Analysis, and Applications*, Applied Mathematical Sciences No. 75 (Springer, Berlin, 1988).
[53] A. Segatti, M. Snarski, and M. Veneroni, Equilibrium configurations of nematic liquid crystals on a torus, Phys. Rev. E **90**, 012501 (2014).
[54] S. Shkoller, Well-posedness and global attractors for liquid crystals on Riemannian manifolds, Commun. Part. Diff. Eq. **27**, 1103 (2002).
[55] G. Napoli and L. Vergori, Equilibrium of nematic vesicles, J. Phys. A **43**, 445207 (2010).
[56] M. Olshanskii, A. Quaini, A. Reusken, and V. Yushutin, A Finite Element Method for the Surface Stokes Problem, SIAM J. Sci. Comput. **40**, A2492 (2018).
[57] P. Hansbo, M. G. Larson, and K. Larsson, Analysis of Finite Element Methods for Vector Laplacians on Surfaces, arXiv:1610.06747.
[58] M. Nestler, I. Nitschke, and A. Voigt, A finite element approach for vector- and tensor-valued surface PDEs, J. Comput. Phys. (in press) (2019), doi: 10.1016/j.jcp.2019.03.006.
[59] W. Freeden and M. Schreiner, *Spherical Functions of Mathematical Geosciences: A Scalar, Vectorial, and Tensorial Setup*, Advances in Geophysical and Environmental Mechanics and Mathematics (Springer, Berlin, 2008).
[60] S. Praetorius, A. Voigt, R. Wittkowski, and H. Löwen, Active crystals on a sphere, Phys. Rev. E **97**, 052615 (2018).
[61] B. J. Gross and P. J. Atzberger, Hydrodynamic flows on curved surfaces: Spectral numerical methods for radial manifold shapes, J. Comput. Phys. **371**, 663 (2018).
[62] O. Mickelin, J. Słomka, K. J. Burns, D. Lecoanet, G. M. Vasil, L. M. Faria, and J. Dunkel, Anomalous Chained Turbulence in Actively Driven Flows on Spheres, Phys. Rev. Lett. **120**, 164503 (2018).
[63] A. Reusken, Stream function formulation of surface Stokes equations, IMA J. Numer. Anal. (2018), doi:10.1093/imanum/dry062.
[64] G. Dziuk and C. M. Elliott, Finite element methods for surface PDEs, Acta Numer. **22**, 289 (2013).
[65] G. Dziuk and C. M. Elliott, Surface finite elements for parabolic equations, J. Comput. Math. **25**, 385 (2007).
[66] G. Dziuk and C. M. Elliott, Finite elements on evolving surfaces, IMA J. Numer. Anal. **27**, 262 (2007).

[67] M. Bertalmio, L.-T. Cheng, S. Osher, and G. Sapiro, Variational problems and partial differential equations on implicit surfaces, J. Comput. Phys. **174**, 759 (2001).
[68] J. B. Greer, A. L. Bertozzi, and G. Sapiro, Fourth order partial differential equations on general geometries, J. Comput. Phys. **216**, 216 (2006).
[69] C. Stöcker and A. Voigt, Geodesic evolution laws—A level-set approach, SIAM J. Imaging Sci. **1**, 379 (2008).
[70] G. Dziuk and C. M. Elliott, Eulerian finite element method for parabolic PDEs on implicit surfaces, Interfaces Free Bound. **10**, 119 (2008).
[71] A. Rätz and A. Voigt, PDE's on surfaces: A diffuse interface approach, Commun. Math. Sci. **4**, 575 (2006).
[72] S. Vey and A. Voigt, AMDiS: Adaptive multidimensional simulations, Comput. Vis. Sci. **10**, 57 (2007).
[73] T. Witkowski, S. Ling, S. Praetorius, and A. Voigt, Software concepts and numerical algorithms for a scalable adaptive parallel finite element method, Adv. Comput. Math. **41**, 1145 (2015).
[74] See Supplemental Material at http://link.aps.org/supplemental/10.1103/PhysRevFluids.4.044002 for simulation videos.
[75] E. Tjhung, D. Marenduzzo, and M. E. Cates, Spontaneous symmetry breaking in active droplets provides a generic route to motility, Proc. Natl. Acad. Sci. USA **109**, 12381 (2012).
[76] W. Marth, S. Praetorius, and A. Voigt, A mechanism for cell motility by active polar gels, J. R. Soc. Interface **12** (2015),
[77] A. J. Chorin, Numerical solution of the Navier-Stokes equations, Math. Comput. **22**, 745 (1968).
[78] H. Mori, E. C. Gartland, Jr., J. R. Kelly, and P. J. Bos, Multidimensional director modeling using the Q tensor representation in a liquid crystal cell and its application to the π cell with patterned electrodes, Jpn. J. Appl. Phys. **38**, 135 (1999).